Turun yliopisto
University of Turku

OBSERVATIONS OF ENERGETIC PARTICLES AND RADIO EMISSIONS DURING MULTIPLE CORONAL MASS EJECTIONS

Firas Al-Hamadani

TURUN YLIOPISTON JULKAISUJA - ANNALES UNIVERSITATIS TURKUENSIS
Sarja - ser. AI osa - tom. 586 | Astronomica - Chemica - Physica - Mathematica | Turku 2018

Turun yliopisto
University of Turku

OBSERVATIONS OF ENERGETIC PARTICLES AND RADIO EMISSIONS DURING MULTIPLE CORONAL MASS EJECTIONS

Firas Al-Hamadani

TURUN YLIOPISTON JULKAISUJA – ANNALES UNIVERSITATIS TURKUENSIS
Sarja - ser. A I osa - tom. 586 | Astronomica - Chemica - Physica - Mathematica | Turku 2018

University of Turku

Faculty of Science and Engineering
Department of Physics and Astronomy

Research Director

Professor Rami Vainio
Department of Physics and Astronomy
University of Turku
Turku, Finland

Supervised by

Research fellow Eino Valtonen
Department of Physics and Astronomy
University of Turku
Turku, Finland

Adjunct Professor Silja Pohjolainen
Tuorla Observatory
University of Turku
Turku, Finland

Dr. Amjad Al-Sawad
Ministry of Higher Education and
Scientific Research
Baghdad, Iraq

Reviewed by

Dr. Juhani Huovelin
Department of Physics
University of Helsinki
Helsinki, Finland

Professor Rodriguez-Pacheco Martin
Department of Physics and Mathematics
University of Alcalá
Madrid, Spain

Opponent

Dr. Alexander Stepanov
Pulkovo Observatory
St Petersburg, Russian Federation

The originality of this thesis has been checked in accordance with the University of Turku quality assurance system using the Turnitin OriginalityCheck service.

ISBN 978-951-29-7315-6 (PRINT)
ISBN 978-951-29-7316-3 (PDF)
ISSN 0082-7002 (PRINT)
ISSN 2343-3175 (PDF)
Painosalama Oy – Turku, Finland 2018

Acknowledgement

All praise be to Allah, the first before the bringing forth and giving of the life and the last after the extinction of all things. The all-knowing who does not forget who remembers him and nor disappoints who supplicates him and nor cuts off the hope of who hopes in him. Praise belongs to Allah the first, without a first before him, and the last, without a last behind him. Praise to Allah for what He has bestowed and thanks for what He has done. O God, bless prophet Muhammad and his household and give us success in this day of ours, this night of ours, and in all our days.

Firstly, I would like to express my deepest gratitude to my supervisor Silja Pohjolainen for her continuous supporting my Ph.D study and related research, for her patience, motivation, and immense knowledge. This support helped me along the way to be on the right track and to take steady steps in scientific research. She gave me the tools and techniques of this science and I would never have been able to finish my dissertation without her guidance.

I am particularly thankful to my supervisor Eino Valtonen, whose encouragement, guidance and support from the initial to the final level enabled me to develop a deeper understanding of the subject. He has been actively interested in my work and has always been available to advise me. I am very grateful for his patience, motivation, enthusiasm, that taken together and make him a great mentor.

I would like to credit my supervisor Amjad Al-Sawad, who gave me this opportunity to complete my doctoral studies in Finland. I have learnt from him the basis of this field and I am so grateful as he was the supervisor during my study on master and doctoral levels.

I would also like to acknowledge the department of physics and astronomy as it has provided the support and equipment I needed to complete my thesis. I would like to thank all my colleagues, including, but not limited to Osku Raukunen, who as a good friend, was always willing to help and give his best suggestions.

I consider myself an extremely lucky person to have so many amazing friends who helped me through this journey. I would like to give a special thanks to Mari Jokinen as she has been very supportive towards my family and me, by providing us with whatever we asked for immediately regardless of any other preoccupation.

I would like to thank my wife, for her understanding and love during the past few years. Her support and encouragement in the end is what made this dissertation possible, she was always cheering me up and stood with me through the good and bad times. I would like to express my deepest gratitude to she who supported me in the days of my weakness, to who loved me since I was young, the best of what I see in myself, the one who changes every moment of pain in my life and turns it to joy, my mother. And finally I would like to show acknowledgement to my inspiration and greatest teacher my father, who I wish could be with me at this moment but paradise was thirsty for him and hastened his departure from this world.

Firas Al-Hamadani

Turku, April 2018

Contents

Abstract

This doctoral thesis studies the characteristics of solar energetic particle (SEP) events and solar radio bursts during multiple coronal mass ejections (CMEs). As well the influences of solar and interplanetary (IP) processes (flare-CME associations, CME-CME interactions, CME-streamer interactions, shock-CME interactions) on the structure of type II radio bursts are investigated.

A series of SEP events with three peaks in the intensity-time profiles within a time interval of $\sim$ 26 hours is analysed. The first event was weak and the proton intensity enhancement was observed only below $\sim$25 MeV. The second particle event was associated with an X1.5-class X-ray flare and a fast and wide CME. The CME had been reported to be radio quiet. The third SEP event occurred about 18 hours later on the tail of the second one, reached proton energies up to $\sim$60 MeV, and lasted for roughly 2 days at energies $>$10 MeV. We found that the first small SEP enhancement was caused by flare acceleration and the following two peaks were produced by shock waves driven by fast CMEs.

A study of SEP events during periods with consecutive solar eruptions originating from a single active region is presented. Each sequence consisted of three consecutive, intense X-ray flares originating from the same active region, each one accompanied by fast halo CMEs, extreme-ultraviolet (EUV) waves and type III and type II radio bursts. The first two eruptions in each sequence were accompanied by clear SEP events, while the third event did not show any measurable SEP enhancement above the background. We suggest that the previously launched interplanetary CMEs and shocks modified the propagation paths of both the electron beams responsible of the type III radio-emission and solar energetic protons. Also the previous eruptions could have reduced the seed population, leading to inefficient particle acceleration.

A statistical study of IP radio type II bursts was carried out to determine the causes of the intense enhancements in their radio emissions. Type II bursts are known to be due to propagating shocks that are often associated with fast halo-type coronal mass ejections. To obtain the directions and heights for the propagating CMEs and the type II bursts, we analysed the radio spectral data and the white-light coronagraph images of our selected events. CMEs preceding the selected events were included in the analysis to verify whether CME interaction was possible. As a result, we found that most of the events were due to shock-streamer interactions, while in some cases CME-CME interaction was the cause of the enhancements.

An unusual solar event consisting of three consecutive CMEs originating from the same active region was investigated. This event was associated with several periods of radio type II burst emission at decameter–hectometer (DH) wavelengths. Based on our data analysis we conclude that the first radio type II burst could have been due to a shock wave launched by a sudden acceleration of the CME2 core and accelerating the CME3, if the plasma densities were very low ahead of the CMEs, or by the accelerating CME1 core if the plasma densities were very high inside the CME1 cavity. The start of the second type II burst at higher frequencies indicates that it was due to a separate shock, propagating to a different direction, within different atmospheric density. The last type II burst period showed enhanced emission in a wider bandwidth, which was most probably due to the CME–CME interactions.

List of publications

I. Analysis of Multi-Eruption Solar Energetic Particle Events (MESEP) on March 17-18, 2003
Firas Al-Hamadani, Amjad Al-Sawad, Eino Valtonen, & Silja Pohjolainen
Proceedings of the 34th International Cosmic Ray Conference, PoS (ICRC2015) 084 (2015)

II. Observations of Solar Energetic Particle Events During Multiple Coronal Mass Ejections
Silja Pohjolainen, Firas Al-Hamadani, & Eino Valtonen
Solar Physics
Proceedings of the 34th International Cosmic Ray Conference, PoS (ICRC2015) 086 (2015)

III. Propagation of Solar Energetic Particles During Multiple Coronal Mass Ejection Events
Silja Pohjolainen, Firas Al-Hamadani, & Eino Valtonen
Solar Physics **Vol. 291**, 487, (2016)

IV. Origin of Radio Enhancements in Type II Bursts in the Outer Corona
Firas Al-Hamadani, Silja Pohjolainen, & Eino Valtonen
Solar Physics **Vol. 292**, 127, (2017)

V. Formation of Radio Type II Bursts During a Multiple Coronal Mass Ejection Event
Firas Al-Hamadani, Silja Pohjolainen, & Eino Valtonen
Solar Physics **Vol. 292**, 183, (2017)

The Author's Contributions to the Included Papers.

Paper I

The manuscript was written by the author, with assistance from the supervisors. The focus of the research was chosen in collaboration with the supervisors. Data analysis and processing was conducted by the author. The interpretation of the results was written with assistance from the supervisors.

Paper II

The focus of the research was chosen in collaboration with the supervisors. The author contributed in the simulations using the ENLIL with cone model and in the interpretation of the data.

Paper III

The focus of the research was chosen in collaboration with the supervisors. Main properties of the data and supportive observations such as electrons data and magnetic field measurements were undertaken by the author.

Paper IV

The manuscript was written by the author and the supervisors. The focus of the research was chosen in collaboration with the supervisors. The data selection, collection, processing, and analyses were conducted by the author. The interpretation of the results was written by the supervisors and the author.

Paper V

The manuscript was written by the author and the supervisors. The main idea of the research was chosen by the author. Data analysis and processing was conducted by the author with assistance from the supervisors. The interpretation of the results was written by the supervisors and the author.

Abbreviations

ACE	Advanced Composition Explorer (NASA satellite)
AR	Active Region
AU	Astronomical Unit
BA	Brightness Asymmetry
CCMC	Community Coordinated Modeling Center
CELIAS	Charge, Element, and Isotope Analysis System (onboard SOHO)
CME	Coronal Mass Ejection
COSTEP	Comprehensive Suprathermal and Energetic Particle Analyzer (onboard SOHO)
CSHKP	Carmichael, Sturrock, Hirayama, Kopp & Pneuman
CTOF	Charge Time-Of-Flight (sensor in CELIAS)
3D	Three-Dimension
DH	Decametric-Hectometric
EIT	Extreme-ultraviolet Imaging Telescope (onboard SOHO)
ENLIL	Time-dependent 3D MHD model of the heliosphere
EPAM	Electron, Proton and Alpha Monitor (onboard ACE)
EPHIN	Electron, Proton, and Helium Instrument (onboard SOHO)
ERNE	Energetic and Relativistic Nuclei and Electrons (onboard SOHO)
EUV	Extreme UltraViolet
FITS	Flexible Image Transport System
FOV	Field-Of-View
GOES	Geostationary Operational Environment Satellite
GSM	Geocentric Solar Magnetospheric coordinates
HED	High Energy Detector (detector telescope in ERNE)
HFR	High Frequency Receiver (STEREO/WAVES receiver)
HISCALE	Heliospheric Instrument for Spectral Composition and Anisotropy at Low Energies (onboard ULYSSES)
HXR	Hard X-Ray
IDL	Interactive Data Language
IMF	Interplanetary Magnetic Field
IP	InterPlanetary
km	kilometer
KSO	Kanzelhöhe Observatory
L1	First-Lagrangian point
LASCO	Large Angle Spectrometric Coronagraph (onboard SOHO)
LED	Low Energy Detector (detector telescope in ERNE)
LDE	Long Duration Event
LFR	Low Frequency Receiver (STEREO/WAVES receiver)

MAG	Magnetic Field Experiment (onboard ACE)
MESEP	Multi-Eruption Solar Energetic Particle
MHD	Magnetohydrodynamic
MTOF	Mass Time-Of-Flight (sensor in CELIAS)
NOAA	National Oceanic and Atmospheric Administration
OA	Outline Asymmetry
OSO-7	7^{th} Orbiting Solar Observatory
PFSS	Potential Field Source Surface model
$R_{\odot}$	Solar Radius
RAD1 & RAD2	Radio Receiver Band 1 & 2 (Wind/WAVES receivers)
RHESSI	Reuven Ramaty High-Energy Solar Spectroscopic Imager(NASA satellite)
RL	Radio-Loud
RQ	Radio-Quiet
RTN	Radial Tangential Normal
S	Symmetry
SDAC	Solar Data Analysis Center
SECCHI	Sun-Earth Connection Coronal and Heliospheric (onboard STEREO)
SEP	Solar Energetic Particle
SOHO	Solar and Heliospheric Observatory (ESA/NASA satellite)
SSW	SolarSoftWare
STEREO	Solar Terrestrial Relations Observatory (NASA satellite)
STEREO/A	STEREO/Ahead
STEREO/B	STEREO/Behind
STOF	Suprathermal Mass Time-Of-Flight (sensor in CELIAS)
SXR	Soft X-Ray
SXT	Soft X-Ray Telescope (onboard Yohkoh)
TDS	Time Domain Sampler (STEREO/WAVES receiver)
TNR	Thermal Noise Receiver (Wind/WAVES receiver)
TOF	Time-Of-Flight
UV	Ultraviolet
VDA	Velocity Dispersion Analysis
WAVES	Radio and Plasma Wave experiment (onboard Wind)
Wind	NASA's satellite
WSA	Wang-Sheeley-Arge model
XRS	X-Ray Sensors (onboard GOES)
XUV	eXtreme Ultraviolet
Yohkoh	"Sunbeam" in Japanese (Japanese satellite)

Chapter 1

INTRODUCTION

1.1 General View of the Sun

The Sun is the largest object in our solar system and contains approximately 99.8% of the solar system mass. It is a luminous ball of ionized gas. The standard solar model assumes that the Sun was created by contracting out of a cloud of gases, which consisted of hydrogen with some helium and heavier elements processed in the Orion Arm, one of the spiral arms of the Milky Way galaxy. The chemical composition of the Sun contains about 70% hydrogen, 28% helium, and 2% heavier elements. The Sun is composed of two major zones, the interior zone and the atmosphere. The interior zone is divided into three layers starting from the center: the core, the radiation zone, and the convection zone, while the solar atmosphere is separated into the photosphere, the chromosphere, and the corona.

Energy is produced at the core of the Sun by nuclear fusion of protons to form helium nuclei. The main process producing energy inside the Sun is the proton-proton chain, where four protons fuse to produce one helium nucleus. In a minor process known as the carbon-nitrogen-oxygen cycle, the protons pass through a series of reactions with heavy elements to produce one helium nucleus.

Still in the forties of the last century, the Sun had been seen only in the visible range of the electromagnetic spectrum. This gave us the view of the photosphere and the low chromosphere where the majority of visible light is produced. With the evolution of human capabilities in space research and monitoring devices, new prospects were opened to observe the other solar layers in different parts of the spectrum and get more information about the characteristics of the Sun, such as the density and temperature.

For example the *Extreme-ultraviolet Imaging Telescope* (EIT) onboard the *Solar and Heliospheric Observatory* (SOHO) operated in four different wavelengths to observe various regions and phenomena in the solar atmosphere (see Figure 1.1): 17.1 nm to observe the corona/transition region boundary; 19.5 nm to observe the quiet corona and coronal holes; 28.4 nm to observe active regions (AR); and 30.4 nm to observe chromospheric network and coronal holes (Delaboudinière et al., 1995).

1.2 Solar Activity

The Sun shows a variety of signs of activity and dynamic behaviour. These signs take many forms, including solar wind, radio wave flux, energy bursts such as solar flares, coronal mass ejections (CMEs), coronal heating and sunspots.

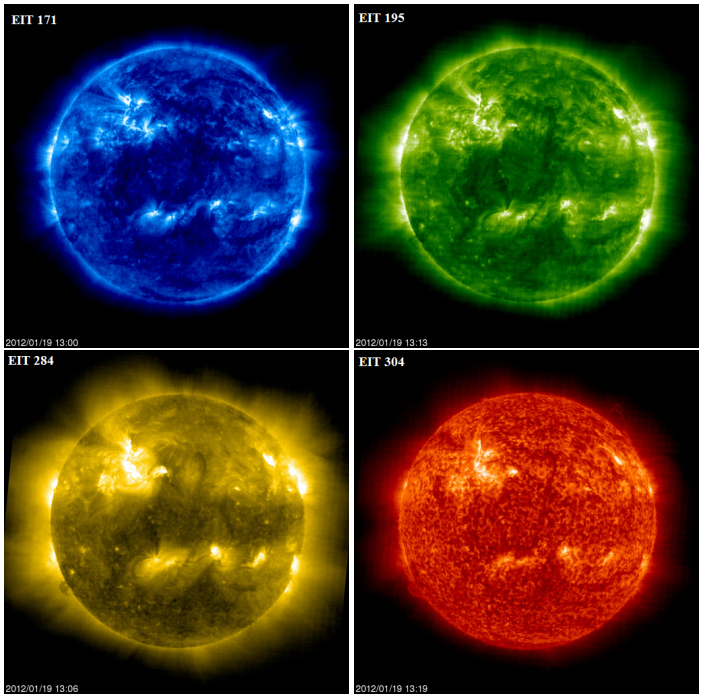

Figure 1.1: SOHO/EIT images of the Sun in different wavelengths on 19 January 2012.

The sunspots are dark irregular shaped areas found on the surface, the photosphere of the Sun. They are characterized by a lower temperature compared to their surrounding areas and intense magnetic field. The average number of sunspots that can be seen on the surface of the Sun is not always the same, but goes up and down in one solar cycle. The periodic rise and fall in the number of sunspots every 11 years was first noted by Schwabe (1844). This cycle is referred to as the sunspot cycle. In the minimum of the solar cycle a few spots can be seen (some times not at all) and most are at relatively high latitudes. As the solar cycle progresses, the number of the spots increases and the sunspots move towards the solar equator. Sunspots usually appear in pairs of opposite magnetic polarity. The magnetic polarity of the Sun changes each solar cycle, with the northern magnetic pole during a cycle turning into a southern pole in the next cycle.

Active regions around sunspots can erupt into powerful solar storms that emit streams of charged particles and magnetized plasma into space. Magnetic activity on the Sun causes disturbances moving out through interplanetary space as a stronger than usual solar wind. Enhanced solar activity, especially coronal mass ejections, solar flares and energetic particles can also produce large fluxes of penetrating energetic protons of great destructive potential. When either of these phenomena arrives near the Earth and strikes a satellite or spacecraft, damage is likely to be done. Astronauts on interplanetary missions, often far off from the Earth-Sun line, will be subject to high energy solar particle events and high energy radiation (X-rays and γ-rays) from solar flares. The interaction of the solar wind and heliospheric magnetic field with the magnetosphere and ionosphere results in variations of the geomagnetic field that induce hazardous electric currents in grounded technological systems such as electric power and hydrocarbon transportation networks, and even increase corrosion in pipelines at high latitudes.

Chapter 2

SOLAR PHENOMENA

2.1 Solar Flares

A solar flare is a sudden and intense increase in brightness observed near the Sun's surface (Hudson et al., 1995). Flares were first observed in 1859 (Carrington, 1859). They emit energy at around $3\times\ 10^{25}$ J (Priest, 1982) over a period of an hour, sometimes extending to a day (Bougeret, 1985). As a comparison, if this amount of energy is projected on the Moon, it could push it about 50 km further from the Earth (Miller, 1998).

A number of studies have been conducted on the solar flares to find out how they emerge and their association with other solar phenomena. Hale (1931) studied the correlation between the large geomagnetic storms and flares. The ionospheric effect was examined by Richardson (1951). Parker (1961) suggested that large solar flares produce shock waves that reach the Earth after a day or two. A large part of the flare energy is in the form of suprathermal electrons and ions, which stay trapped at the Sun and produce a wide variety of radiations (Ramaty & Murphy, 1987), as well as escape into interplanetary (IP) space (Reames, 1990). The radiation from trapped particles consists in general of (1) continuum emission, which ranges from radio and microwave wavelengths to soft ($\sim$ 1–20 keV) X-rays, hard ($\sim$ 20–300 keV) X-rays, and finally γ-rays (above $\sim$ 300 keV), which may have energies in excess of 1 GeV; (2) narrow γ-ray nuclear de-excitation lines between $\approx$ 4 and 8 MeV; and (3) high-energy neutrons observed in space or by ground-based neutron monitors. The particles that escape into space consist of both electrons and ions, which often have compositions quite different than that of the ambient solar atmosphere.

It is believed that chromospheric evaporation pushes the upflow of heated plasma into flare loops. This process generates steep density gradients at the upflow front. The density is considered to be the key to different physical processes that evolve during solar flares. The flare's electron densities can be measured by different methods such as the plasma frequency of coherent radio emission, soft X-rays (SXR) or X-ray/ultraviolet (XUV) emission, density-sensitive line ratios (e.g., Doschek, 1990), line width of the higher Balmer lines (e.g., Foukal et al., 1983), and intensity of the electron scattering (white light) continuum for limb flares (Ichimoto et al., 1992).

2.1.1 Solar Flare Types

Solar flares are usually classified according to different features, particularly, their duration, area, geometric shape, brightness in different bands of the electromagnetic emission, presence of plasma bursts, their parameters on the Sun and in the interplanetary medium, etc. The two

most widely used classification systems (Table 2.1) classifies flares according to their size or importance. The first classification was developed during the 1930s based on observation of the Hα spectral line. Hα is a spectral line of neutral hydrogen (red part of the electromagnetic spectrum) in the Balmer series with a wavelength of 656.28 nm. It results from the transition of the hydrogen electron from the third to the second energy level. As a result of this transition the atom emits Hα light. Hα measurements can be divided into the classes S, 1, 2, 3, and 4 according to the area of the flaring region on the solar disk, where S refers to sub-flares. Hα intensity can be further classified in sub-categories by brightness: f-faint, n-normal, b-bright. The most distinct flares are classified as 4b and the smallest and faintest as Sf . The second classification developed in 1970, describes the X-ray peak flux in the wavelength range 1 – 8 Å. Flares are classified into five types (A, B, C, M, X), where the letters designate the order of magnitude of the peak flux. A number following the letter is the multiplicative factor. For example, C9.3 flare refers to an X-ray peak of 9.3 $\times 10^{-6}$ Wm $^{-2}$. The X-ray flux classification has been adopted by the *Geostationary Operational Environment Satellites* (GOES).

Table 2.1: Solar flare classification

Soft X-ray class		Hα classification	
class	Intensity [Wm^{-2}]	class	Area 10^{-6} solar disk
A	$10^{-8} - 10^{-7}$	S	200
B	$10^{-7} - 10^{-6}$	1	200 – 500
C	$10^{-6} - 10^{-5}$	2	500 – 1200
M	$10^{-5} - 10^{-4}$	3	1200 – 2400
X	$> 10^{-4}$	4	> 2400

Flares are also divided into two types, gradual and impulsive (e.g., Cliver, 1996) according to the temporal profile of the soft X-ray emission.

2.1.2 Solar Flare Models

Solar flares may have three stages: (a) precursor phase, (b) impulsive phase and (c) decay phase. The precursor phase begins when the magnetic energy is released. The associated emission with this phase is SXR. In impulsive phase, energetic charged particles (primarily protons and electrons) are accelerated to energies exceeding 1 MeV. Radio waves, hard X-rays (HXR), and γ-rays are emitted during this phase. The decay phase occurs when the gradual build up and the decay of SXR is detected.

There is a strong tendency for sunspots to occur in pairs or groups and normally connected with magnetic loops with the foot points anchored to each of the spots in a sunspot group. These loops will fill up with charged plasma which makes them visible to instruments that can detect the light from these gases. The loops become distorted and stretched, because the magnetic field distortion can happen when another sunspot group collides with the first one, or a new sunspot group forms between the pairs of the current group. This temporarily generates a lot of magnetic stress. At some point during the pre-flare changes, oppositely-directed magnetic field lines are dragged by gas motions into smaller and smaller volumes of space. It is well known in the science of electricity and magnetism that if you have opposite-directed magnetic field lines, a current is generated in the space between them by induction. These currents, in a pre-solar flare region, appear within the charged plasma that was originally present near the magnetic loops. As the opposing field lines get closer, these currents of gas become more and more

intense. The gas currents generate heat because the ions collide with neutral atoms in the gas which provides resistance to the current flow. This process takes less than an hour, and in most cases the friction heats the gases to temperatures of millions of degrees. Over a short time, the gases emit more and more energetic forms of X-rays and then γ-rays. The X-ray spot begins to grow in intensity. Similar spots can appear near the footpoints of the original magnetic loop. This process eventually subsides over the course of a few minutes. Meanwhile as the currents are growing in strength near the magnetically-opposed region, the magnetic lines break and reconnect in a new shape as the stored magnetic energy is lost to heating the local gases. The new magnetic shape, if enough energy is available, can drag its own trapped clouds of plasma away from the sunspot flaring region and cause a brief, but powerful, ejection of matter into the solar corona and beyond. The largest of these ejections are called coronal mass ejections. Only the most powerful solar flares are capable of launching these billion-ton clouds of gas into interplanetary space, although it is sometimes possible for a large number of smaller flares to make this happen as well. The intensity of the flare, and the energies of the particles that have been emitted during reconnection, begin to wane in strength as the new magnetic field shape starts to relax into a less distorted shape (see Holman et al., 2006, and references therein).

The standard model of eruptive flares that has been developed by Carmichael (1964), Sturrock (1966), Hirayama (1974), and Kopp & Pneuman (1976) is also called the CSHKP model. This model describes the long duration event (LDE) flares or cusp-type flares. The CSHKP model suggests that the coronal reconnection of magnetic fields occurs at the top of the cusp loop system. The accelerated particles are directed downwards to the base of the chromosphere and produce radiation in the HXR part of the electromagnetic spectrum. Hα is also produced as a result of recombination of ionized hydrogen atoms. This procedure occurs so fast, that the plasma is not in thermodynamic equilibrium. The Hα emission begins in small kernels, which speedily passage out in the shape of flare ribbons on either side of the magnetic polarity inversion line. At the thermodynamic equilibrium, hot plasma expands quickly and fills the coronal loops and emits SXR. Thus, SXR emission begins simultaneously with Hα flare and HXR rise, but SXR peak emission occurs a little later, when the entire loop is filled and starts cooling (Magara et al., 1996).

Figure 2.1 is a simplified cartoon of CSHKP model and explains the features of solar flares observed in Hα, soft and hard X-rays.

2.2 Coronal Mass Ejections

Coronal mass ejections (CMEs) are huge bubbles of gas threaded with magnetic field lines that are ejected from the Sun over the course of several hours. They are capable to release tremendous amounts of magnetized plasma into IP space (Howard et al., 1985) about $\sim 10^{13}$ – 10^{16} g (Vourlidas et al., 2010) with velocities $\sim$100 – 3000 km s^{-1} (e.g., Yashiro et al., 2004). They were discovered for the first time in the seventies of the last century in the era of Skylab 1973 – 1979 (Gosling et al., 1974) and the *7th Orbiting Solar Observatory* 1971 – 1973 (OSO-7) (Tousey, 1973; MacQueen et al., 1974). Hundhausen et al. (1984) first defined a CME as a white light feature observed in a coronagraph's field of view, accompanied by significant changes in the composition of coronal structures that happened on a time scale of a few minutes and several hours.

CMEs are associated with flares, filament eruptions, shocks, radio bursts, and solar energetic particle (SEP) events. Typical CMEs (Figure 2.2) have three structural components: the front, the cavity, and the core (Illing & Hundhausen, 1983).

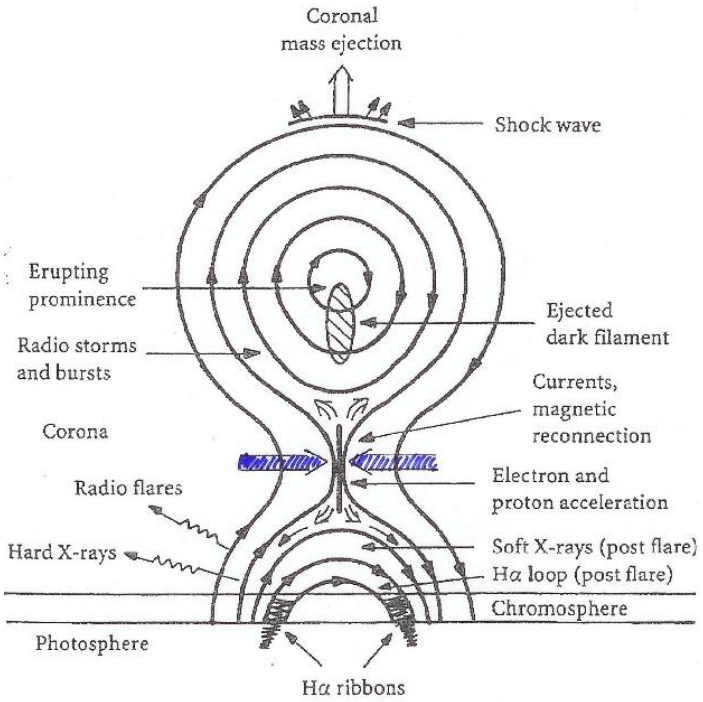

Figure 2.1: Schematic diagram of a large eruptive flare. The CME forms from the ejected filament and drives a shock wave if the CME has a speed that exceeds the ambient solar wind. (Lang, 1995)

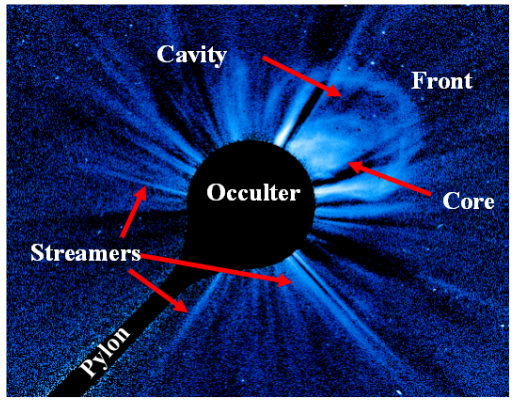

Figure 2.2: The figure illustrates a typical CME with the three part structure and other coronal structures like streamers. The image was retrieved from `https://hesperia.gsfc.nasa.gov/summerschool/lectures.html`

2.2.1 CME Types

Different studies report two kinds of coronal mass ejections, gradual and impulsive (e.g., Sheeley et al., 1999; Srivastava et al., 1999; Švestka, 2001; Moon et al., 2002). These studies suggest that the gradual CMEs are accelerated slowly across great distances with speed ranges of about

300 to 600 km s^{-1}. The impulsive CMEs occur lower in the corona and are accelerated up to speed range around 2000 km s^{-1}. The impulsive CMEs are found to be associated with solar flares, while the gradual CMEs occur during solar minimum and are especially associated with prominences (Schwenn et al., 2005).

Based on the data from space-based coronagraphs, CMEs distinctly appear in triple forms (Figure 2.3):1) Halo CMEs appear when the angular width is 360° and occur near to the disk center and predominantly appear to encircle the occulting disk of the coronagraph (Howard et al., 1982). Also there is a sub-classification of halo CMEs according to their heliocentric distances and brightness as S-symmetry, BA-brightness asymmetry, and OA-outline asymmetry. 2) Partial halo CMEs appear when the angular width is between 120° and 360°. 3) Limb CMEs occur above the limb and have an angular width less than 120°. It is worth mentioning that the angular width represents the angular breadth of the CMEs, which is measured from the white-light images of a coronagraph (Gopalswamy et al., 2004).

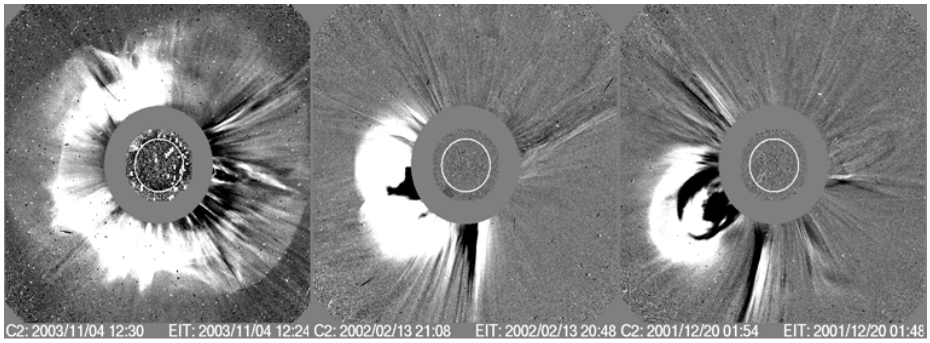

Figure 2.3: SOHO/ LASCO images showing the three CME types. The left panel shows a full halo CME observed on 04 November 2003, the middle panel shows a partial halo CME on 13 February 2001, and the right panel a limb CME observed on 20 December 2001.

2.2.2 CME Models

Several CME models have been proposed to explain the pre-eruption structures, their initiations, and their eruptions. In the following, we summarize a few of them. The *break-out model* (Figuer 2.4), was developed by (Antiochos, 1998; Antiochos et al., 1999). The magnetic break out model of CME initiation is based on a sheared quadrupolar magnetic structure. The non-potential magnetic field of a filament channel, is a sheared arcade and the reconnection above the filament channel causes the eruption. The eruption is driven by shearing of the footpoints of the local bipolar region around its neutral line. As a result, the local bipolar field inflates and begins to reconnect with the oppositely orientated overlying field. This reconnection transfers overlying field to the side lobes, until the CME erupts through the weakened overlying field. The location of magnetic reconnection that drives this type of CME initiation model occurs above the CME flux rope.

The *tether cutting model* (Moore et al., 2001) (Figure 2.5) is based on a single bipolar field geometry. The event onset is due to reconnection of two inner legs of a sigmoidal magnetic structure, which produces low-lying shorter loops across the magnetic polarity inversion line and longer twisted loops linking the two far ends of the sigmoid. The second stage begins when the twisted loops become unstable and erupt outward, distending the overarching envelope field.

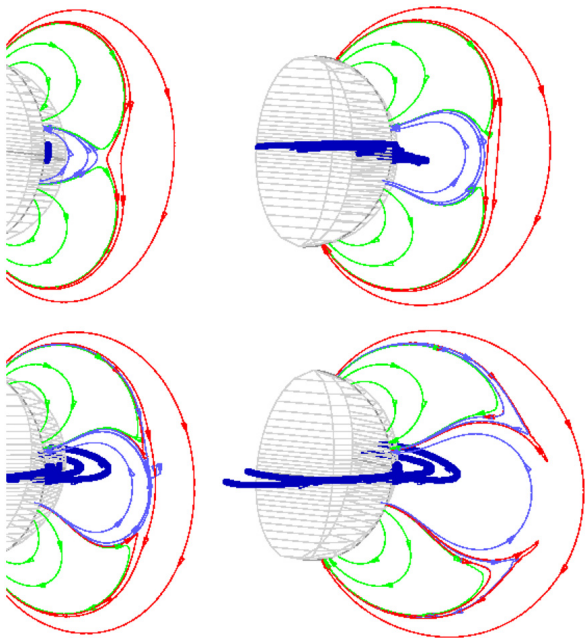

Figure 2.4: The evolution of the magnetic field in the break-out model (taken from Antiochos et al. (1999)).

The opened legs of the envelope field subsequently reconnect back to form an arcade structure with bright ribbons at their footpoints, and the ejected flux rope escapes as a CME (Liu et al., 2013).

The magnetic field in the *flux-injection model* is a flux rope with foot points grounded under the photosphere. An eruption like this can be achieved through flux injection process or upsurge in poloidal flux. This process is highly effective in producing not solely the observed features near the Sun, but also in the IP medium (Krall et al., 2000).

2.3 Streamers

Coronal streamers are the brightest dense semi-fixed structures, visible either in white light or ultraviolet (UV) extending from the solar surface to IP space (see Figure 2.2). The streamers usually have much higher plasma density than the surrounding medium, so that the Alfvén speed is lower than in the surroundings and the plasma influx is slow and barely measurable in the closed magnetic field (Habbal et al., 1997; Strachan et al., 2002; Kwon et al., 2013; Chen, 2013). Streamers are constantly interacting with CMEs (e,g., Howard et al., 1985; Hundhausen, 1993; Chen et al., 2010, 2011; Feng et al., 2011; Chen, 2013). Many studies report that interactions between CME shock and streamers could be possible sources of metric and IP type II bursts (e.g., Reiner et al., 2003; Cho et al., 2007, 2011; Kong et al., 2012; Shen et al., 2013; Chen et al., 2014). These studies revealed two types of results. Firstly, the streamer has a high density region with slow plasma outflow and Alfvén speed. Therefore, it is expected that in the streamer region the shock could easily have a super-Alfvénic speed. Secondly, when the shock is facing a streamer from the flank, the shock geometry will be quasi-perpendicular. In both cases the acceleration of electrons at the shock is efficient.

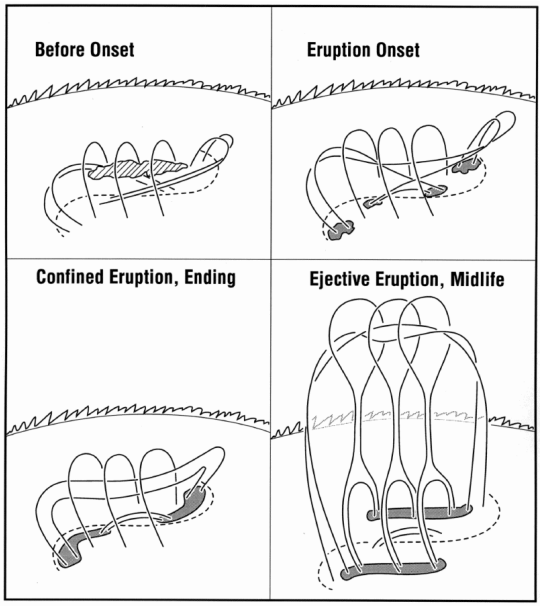

Figure 2.5: The standard model of the magnetic field explosion in single-bipole eruptive solar events. Figure from (Moore et al., 2001).

2.4 Relations Between Solar Eruptions

2.4.1 CME and Flare Association

The relationship between solar flares and coronal mass ejections is a controversial issue in solar physics. It has been observed that CME eruptions appear simultaneously with flares and prominences (Munro et al., 1979; Webb & Hundhausen, 1987). The eruptive flare scenario is the most commonly used model to interpret the connection between flares and CMEs (e.g., review by Priest & Forbes, 2002). The magnetic field lines start to elongate and form a vertical current sheet below the eruption, because of the flux rope elevation. The magnetic energy strengthens the solar flare when the reconnection of magnetic field lines starts in the current sheet. Moreover, the latterly reconnected field lines add poloidal magnetic flux to the rising flux rope, and therefore maintain the upward driven force (Vršnak, 2008). Therefore, the energy emitted from the reconnection process is distributed to boost the kinetic energy of the CME flux rope and to drive dynamic processes in the associated flare.

The flare occurrence rate is much larger than that of CMEs because not all flares are associated with CMEs (e.g., Zhang et al., 2001). The result of the statistical study provided by Moon et al. (2002) proposed that the most powerful flares are associated with the fastest CMEs. Kahler (1992) claimed that 40% of the CMEs are associated with Hα flares. Yashiro et al. (2006) showed that the association rates of CMEs with soft X-ray flares increases with increasing flare size. It was about 40% for M-class flares and 90% for X-class flares. The spatial and temporal relations between CMEs and flares have been studied in details. The CME onset typically precedes the related X-ray flare onset by several minutes (Michalek, 2009).

The CME development includes three phases: the slow rise phase, the impulsive phase, and the propagation phase (Zhang et al., 2004). There is a synchronization process between rapid

CME acceleration and the rising phase of the associated SXR bursts (Zhang et al., 2001, 2004; Gallagher et al., 2003; Vršnak et al., 2004a). As well, the flare passes through three stages, including the pre-flare phase, rise phase, and decay phase. The relationship between the flare evolution phases and the corresponding CME development stages was found by Zhang & Dere (2006). In addition, Temmer et al. (2008, 2010) found a good conjunction between the flare HXR peak and the CME acceleration peak.

2.4.2 CME-CME Interaction

In general the CME interactions occur between two or more CMEs launched from the same or nearby active regions. This phenomenon has been investigated for the first time by Gopalswamy et al. (2001b, 2002a). The optical evidence of CMEs interacting in the corona and IP space was provided by the white-light coronagraph images from the *Solar and Heliospheric Observatory/Large Angle Spectrometric Coronagraph* (SOHO/LASCO). Gopalswamy et al. (2001b) and Burlaga et al. (2002) suggested that during the interaction process, CMEs may merge and propagate as a single magnetic structure. Gopalswamy et al. (2002a, 2004) concluded that the type II radio emission is enhanced and modified due to the interaction between two CMEs. Gopalswamy et al. (2001b) suggested that the observed radio enhancements were produced by the increased density in the upstream medium that reduced the Alfvén speed and therefore increased the Mach number of the shock. Gopalswamy et al. (2001b) pointed to the possibility of electron acceleration in the reconnection between the two CMEs.

The paradigm of CME interaction suggests that the primary CME is faster than the earlier one, catching up with the preceding slower CME. The enhanced radio emission is interpreted as a result of the shock strengthening when it is passing through the dense material of the slow CME. Gopalswamy et al. (2002b) suggest that CME-CME interactions are connected to SEP events. Most interacting CMEs are associated with DH type II radio bursts. Martínez et al. (2012) and Temmer et al. (2012) studied an interacting event on 01 August 2010 and suggested that the associated type II burst radio emission was related to the CME-interaction. In an event examined by Maričić et al. (2014), an increase of the earlier CME speed and decrease of the primary CME speed was found after the interaction.

Chapter 3

SOLAR ELECTROMAGNETIC AND PARTICLE RADIATION

The differences in the temperatures of the solar atmosphere play a significant role in observing the various layers of the Sun in different wavelengths. The photosphere can be seen in white light (T≈6 $\times 10^3$ K), while the chromosphere is observed in UV where the temperature is $\sim$ 10^4 K. In the corona where the temperature reaches $\sim$ 10^5 K the extreme ultraviolet (EUV) wavelength is used for observations, while the X-rays observe the hottest region of the corona, with temperature about $\sim$ 10^6 K.

Radio waves can be produced by multiple mechanisms such as bremsstrahlung emission (free-free emission), gyro-synchrotron emission, plasma emission, and gyroresonance. One or more mechanisms can occur at the same time in the Sun.

3.1 X-rays

The solar surface temperature is about 6000 K. At this temperature the Sun should be unusually weak source of X-rays. However, the Sun is a very strong X-ray emitter. The explanation is that the source of X-rays is not at the surface of the Sun, but in the corona. The temperature of the corona reaches millions of degrees, and the hot plasma (i.e. ionised gas) emit X-rays.

X-ray wavelengths lie between UV and γ-rays on the electromagnetic spectrum with wavelengths between 10^{-9} – 10^{-12} meters. Because X-rays cannot penetrate the Earth's atmosphere, they must be observed in space. X-rays are sub-divided into soft and hard X-rays, the approximate borderline between the two types being around 100 picometers or around the energy level of 10 keV per photon.

3.1.1 Soft X-rays

Since the seventies of the last century to present day, solar flares have been assorted according to their soft X-ray peak fluxes (see Table2.1). The class A is the lowest X-ray flux and the class X is the highest. For example the GOES satellites provide fluxes at two broad wavelength bands, 1–8 Å (12.5–1.5 keV) and 0.5–4 Å (25–3 keV).

The SXR emission contains continuum and line emissions, which are formed as a result of several processes. The processes that produce SXR continuum spectrum are bremsstrahlung (free-free transitions), radiative recombination (free-bound transitions), and two-photon decay (Gronenschild & Mewe, 1978). The line emission is produced by electron collision excitations and decays (Landini & Monsignori Fossi, 1990).

3.1.2 Hard X-rays

The hard X-rays have higher energy and shorter wavelength than soft X-rays. It is generally believed that the energy release occurs in the reconnection region and that particles are accelerated along the field lines in upward and downward directions. The downward acceleration produces HXR (see Figure 2.1). The HXR are considered as a good source of information from which we can understand the process of energy release and the mechanism of particle energization during a flare (Dennis, 1988).

3.2 Ultraviolet Radiation

The ultraviolet emission (UV) is electromagnetic radiation with wavelength range roughly from 10 to 400 nm. The wavelength is shorter than visible light and longer than X-rays. About 10% of the total radiative output of the Sun is emitted in UV. The UV is divided to near ultraviolet, far ultraviolet, and extreme ultraviolet.

3.3 Radio Emissions

We have shown in Chapter 2 that the rapid release of energy in the solar corona is defined as a solar flare, and the large-scale bursts of plasma and magnetic field from solar corona to IP space are known as CMEs. These amounts of released energy lead to accelerated particles and emission of electromagnetic radiation almost in all wavelengths. Among those wavelengths, the radio emissions cover the frequency range from a few tens of kHz up to hundreds of GHz. The solar radio emissions based on dynamic spectrum are classified to five types (Figure 3.1): type I, type II, type III, type IV, and type V.

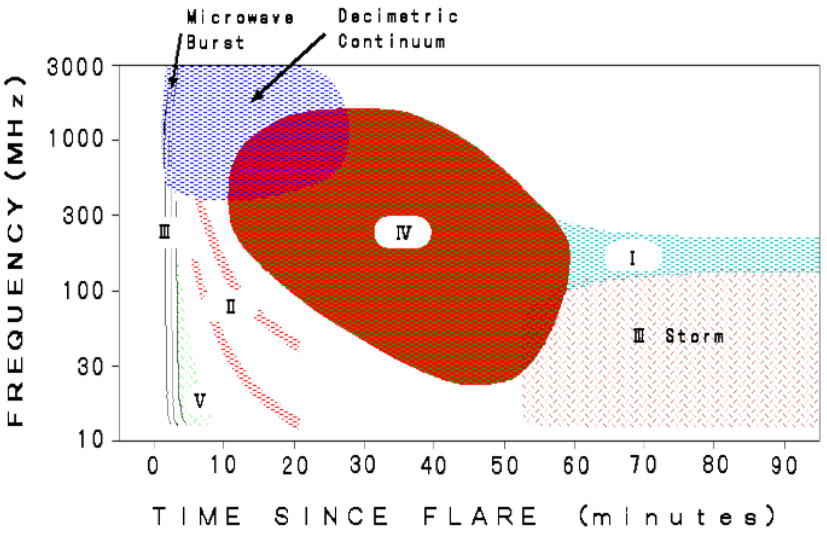

Figure 3.1: The schematic diagram of solar radio emission types showing the radio bursts classification from centimetre to decametre wavelengths. The image was retrieved from `http://sunbase.nict.go.jp/solar/denpa/hiras/types.html`.

3.3.1 Radio Type I Bursts

Radio emissions in metric wavelengths are produced by accelerated non-thermal electrons in the corona. The type I radio bursts, also known as noise storms are the most common phenomena at these wavelengths. There is a common belief that the coronal non-thermal electrons that excite plasma waves are trapped in the closed magnetic loops. The plasma waves are turned into O-mode radio and finally observed as type I (e.g, Mercier et al, 1984). Type I radio bursts are found to be associated with active regions, but not related to solar flares. The burst lasts for hours and sometimes for days. The radio type I can be identified by two different components: one is a long-lasting wide-band continuum component with relatively weak brightness, the other is a very narrow band component of high brightness temperature (Wild et al., 1963).

3.3.2 Radio Type II Bursts

Type II bursts are frequency-drifting plasma radiation produced by shock-accelerated electrons and the emission is observed near the local plasma frequency and/or its harmonics (e.g., Nelson & Melrose, 1985). The observational clues have highly reinforced that the IP type II radio bursts have their source in the foreshock of CME-driven shock waves (e.g., Reiner et al., 1998b).

Quantitative theories have been developed to explain how radio emission is created by propagating shocks and electron beams. Knock et al. (2001, 2003) have attempted to construct a unified model of type II bursts by incorporating available analytic theories and observations. Cairns et al. (2003) summarize and review the theory for type II bursts formulated by Knock et al. (2001, 2003) and the related work of Kuncic et al. (2002a,b). The theory is an analytic, quantitative description of type IIs with four stages. In the first stage, the electrons are reflected and accelerated at the shock, with the configuration including both the shock magnetic mirror and the electrostatic cross-shock potential (Kuncic et al., 2002a). In the second stage, electron beams are formed in the upstream foreshock area by time-of-flight effects (Filbert and Kellogg, 1979; Cairns, 1987). In the third stage, the electron beams supply free energy to push Langmuir waves in the electron foreshock. The stochastic growth theory describes the transformation of free energy into Langmuir waves. In the fourth stage, Langmuir waves interact to produce radio emission by nonlinear wave-wave processes (Robinson et al., 1994; Cairns et al., 2000).

Magnetohydrodynamic (MHD) shocks are observed in association with type II radio bursts in metric (m) wavelengths (e.g., Wild & McCready, 1950; Uchida, 1960; Nelson & Melrose, 1985; Gopalswamy et al., 2005), decametric-hectometric (DH) wavelengths (Gopalswamy et al., 2001a), and kilometric (km) wavelengths (Cane et al., 1987). Metric wavelengths are the earliest signature of a shock in the corona, observed by ground-based telescopes with frequency range 300 – 30 MHz. Type II emission in DH wavelengths is observed only by space-based radio telescopes, because radio emission at frequencies below the ionospheric cutoff cannot penetrate Earth's ionosphere. Type II bursts are observed by e.g., Wind/WAVES in the frequency range 20 kHz – 14 MHz corresponding to DH and km wavelengths (Reiner et al., 1998a; Kaiser et al., 1998; Gopalswamy et al., 2004).

Figure 3.2 shows the variants of type II radio bursts occurring in the Sun-Earth connected space. The red line refers to m-domain originating when the CMEs are at height ~ 2 $R_\odot$ from the center of the Sun. The green lines refer to bursts staring in DH domain and continuing to km domain. The blue line refers to bursts counterparts in all wavelengths m-to-km. The km-type II occurs below 1 MHz, when the CMEs are at heights > 20 $R_\odot$. The average CME speeds for each type of the radio bursts are shown near the burst lines (Gopalswamy, 2010).

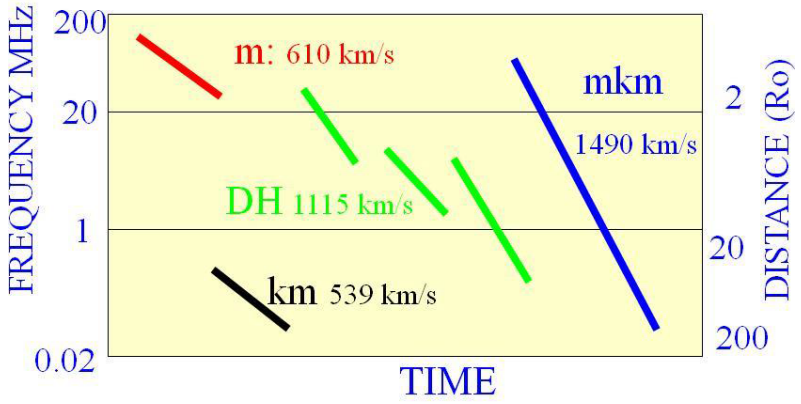

Figure 3.2: Schematic plot of dynamic radio spectrum showing different type II bursts restricted to various wavelength ranges. Figure from (Gopalswamy, 2010).

It has been established that all type II bursts are associated with flares and/or CMEs (e.g., Cliver et al., 1999). The shock waves were used to distinguish between the above types of radio bursts in different wavelengths. The radio type II in metric wavelengths arise in the corona from CME-driven shocks, or from blast waves due to flare eruptions. The association between CMEs and m-type II remains a subject of debate (Gopalswamy et al., 1998; Cliver et al., 1999; Vršnak & Cliver, 2008). Sheeley et al. (1984) agreed with the hypothesis which assumes that the m-type II bursts are generate by blast waves. Vršnak (2001) detected a good correlation between solar flare features and radio type II parameters.

Klassen et al. (1999) found the type II precursor signatures occurring during the onset of impulsive flares in the active region loops. The type II precursor signatures can be defined as the sequence of fast-drift bursts whose overall frequency envelope drifts at a normalized drift rate similar to the subsequent type II burst (Klassen & Pohjolainen, 2002). Another definition for type II precursor signatures has been postulated by Vršnak & Lulić (2000) as an emission from the boundary of an explosive expanding flare volume.

In some cases of type II-CME events there is no clear correlation between the calculated radio burst speeds and burst heights with the CME speeds and CME front heights (e.g., Vršnak et al., 2006; Cho et al., 2007; Kim et al., 2009). This is due to two reasons: either because of projection effects of the white-light CME structures and/or uncertainty of density assessment for the type II burst emissions. Reiner et al. (1997, 1998b) suggest that the source regions of the type II radio emissions are formed at the upstream of the CME driven shocks. Bale et al. (1999) confirmed the source region of the type II emissions by in situ observations. Cho et al. (2011) indicate that the CME nose and CME-streamer interaction could be the source of type II emissions.

Type II in DH and km wavelengths range are caused by electron beams accelerated by CME-driven shocks (e.g., Sheeley et al., 1985; Reiner et al., 1998a; Bale et al., 1999). The halo CMEs associated with DH-type II are more energetic than those associated with m-type II (Gopalswamy et al., 2000; Lara et al., 2003; Shanmugaraju et al., 2003), and more geo-effective (Gopalswamy, 2011). Reiner et al. (2001) claimed that there is a relation between the deduced speeds of DH radio type II and speeds of the CMEs.

The CMEs associated with type II radio bursts are said to be radio-loud CMEs (RL), while those without type II association are called radio-quiet (RQ). There is a high probability of RL

events to drive shocks at Earth. Gopalswamy et al. (2008, 2010) found that 66% of IP shocks were associated with radio type II bursts, while 34% were not. There are a lot of RL-CMEs arising near to the center of the solar disk, but they do not produce shocks at Earth. On the other hand, some of the RQ-CMEs provide a shock signature at Earth (Gopalswamy et al., 2010).

Usually, type II bursts are observed as narrowband and patchy emissions in the IP space, which at intervals can disappear completely (e.g., see, Pohjolainen et al., 2013) . Also type II bursts can be observed as a wide-band emissions in the IP space. Bastian (2007) proposed that type II wide-band emission could be a synchrotron emission from trapped electrons within the CME structure. This means that the type II would not be plasma emission. Recently Pohjolainen et al. (2013) suggested that the wide-band type II bursts are associated with fast halo CMEs. They found 72 % (18 out of 25 events) of the bursts to have heights corresponding to the CME leading front suggesting that they were produced by the bow shock ahead of CMEs. The remnant events were found to have heights much less than CME fronts and reveal a different type of height-time evolution.

The dynamic spectra of type II contain two or more lanes (e.g., Robinson & Sheridan, 1982). The lower frequency band and the higher frequency band are emissions at fundamental (f_p) and second harmonic ($2f_p$) of local plasma frequency, respectively, given by $f_p = 9000\sqrt{n_e}$ [kHz]. Sometimes the type II lane is observed with band splits in both fundamental and harmonic. Band splitting being a results of plasma emission from upstream and downstream shock region (Smerd et al., 1974; Nelson & Robinson, 1975; Vršnak et al., 2001). This assumption has been recently confirmed by Zimovets et al. (2012) and Zucca et al. (2014).

3.3.3 Radio Type III Bursts

Radio type III bursts are the most common types of solar radio emissions. They usually last a few seconds, and are fast drift bursts ($\sim$100 MHz s^{-1} in the meter wave range) from high to low frequencies in the dynamic spectrum (e.g., Suzuki & Dulk, 1985). The starting frequencies of type III bursts differ significantly from burst to burst. In massive solar flares the type III bursts start at GHz frequencies (e.g., Benz et al., 1992). Type III radio bursts are believed to be generated by energetic electron beams accelerated during flares and propagating along open magnetic field lines from the corona into the IP space (see, e.g., Reid & Ratcliffe, 2014, for a review). The electron beams drive Langmuir waves at the local plasma frequency and some of them convert into electromagnetic radiation at the fundamental frequency and/or its second harmonic.

There are two sub-types of type III bursts, J and U shapes, observed in the inner corona where the closed magnetic field lines are widespread. These components occur due to propagating electron beams through curved or closed field lines. In IP space the type III bursts can be classified into three broad types : 1) isolated type III bursts, 2) complex type III bursts, and 3) type III storms. The isolated type III bursts originate from flares and small-scale energy release sites of the Sun. Complex type III bursts are associated with CMEs, and produced by low energy electrons passing through open field lines. The type III storms contain series of short-lived type III bursts in rapid succession (e.g., Fainberg & Stone, 1970). It is believed that the type III storms are produced by electrons from small scale and almost continuous energy release into the closed magnetic structures of active regions.

3.3.4 Radio Type IV Bursts

Type IV bursts are broadband continuum emissions observed in the metric to decimetric wavelength range, and can be classified into two categories of moving type IV and static type IV bursts (Weiss, 1963; Melrose, 1980). Type IV bursts can sometimes be observed in the IP space at DH wavelengths (Hillaris et al., 2016). Type IV bursts are generated by non-thermal electrons trapped in magnetic structures like loops, plasmoid structures, and magnetic arches (e.g., Stewart, 1985). Many mechanisms have been suggested for the radio emission, of which the synchrotron and gyro-synchrotron emissions (e.g., Bastian et al., 2001), the plasma emission (e.g., Ramesh et al., 2013), and the electron cyclotron maser emission (e.g., Winglee & Dulk, 1986) are the most common.

3.3.5 Radio Type V Bursts

Type V bursts are wide bandwidth continuum emissions lasting about one to three minutes, and occurring at frequencies below 150 MHz. They instantly follow type III bursts or type III burst groups (Wild et al., 1959). In general the duration of type V bursts increase with decreasing frequency, with an average range from $\sim$40 s at 200 MHz to $\sim$200 s at 20 MHz. Type V bursts and earlier type III bursts are located at the same height. However, type V sources are usually displaced from type III source by a few tenths of a solar radius or more. As well, the source size of type V radiation is generally larger than that of type III, and increases greatly as frequency decreases (Tang et al., 2013).

3.4 Solar Energetic Particle Events

Solar energetic particle (SEP) events are the most interesting phenomena in solar physics. They introduce radiation risk for space missions in the IP space and causes elevated radiation dose rates for humans in space and high altitudes in the atmosphere and changes in the ionosphere, that cause various effects, including high frequency radio blackouts at polar airline routes. By the end of the 1990s, a two-class picture of SEP events had emerged (see Fig. 3.3). According to this classification the gradual events occur as a result of diffusive acceleration at CME-driven coronal and/or IP shocks, while the impulsive events were attributed to acceleration during magnetic reconnection in solar flares (e.g., Reames, 1999, 2013).

The impulsive events are compact, take place in the low corona, have short durations of several hours, are closely associated with solar flares and accompanied with type III radio bursts, and show large abundance enhancements in the heavy ions. The ratio of ^{3}He/^{4}He$\sim$1, and they also have smaller enhancements of Ne, Mg, Si, and Fe relative to ^{4}He, C, N, and O (Reames et al., 1994). Most impulsive events originate from the western hemisphere of the Sun and have ion time-intensity profiles peaking near the onset times of the associated flares (e.g., Cane et al., 2006).

The gradual events are accelerated in CME-driven coronal and/or IP shocks. They have the following characteristics: occur high in corona, typically last for several days to a week, are associated with SXR and HXR, and type II and type IV radio emissions, have abundance ratios and charge states typical for the solar corona and solar wind, and are electrons-poor and protons-rich. Gradual SEP events are produced by wide and fast CME-driven shocks (Gopalswamy, 2003) and have a wide range of source longitudes (Reames, 1999, 2013).

Some events possess characteristics of both types (gradual and impulsive) (e.g., Kocharov & Torsti, 2002), and this is contrary to what has been claimed by Reames (2002). These events

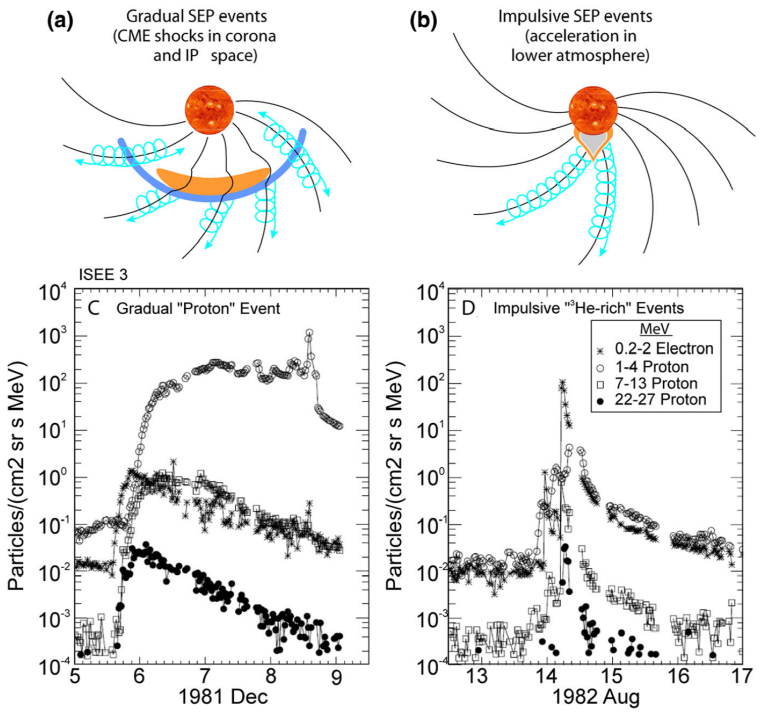

Figure 3.3: The sources of SEP evens in the two-class picture. Figure from Desai & Giacalone (2016).

are called hybrid or mixed events and they challenge the two-class classification of SEP events. The hybrid events may look like gradual events but demonstrate the properties of impulsive ones (Vainio et al., 2007). Papaioannou et al. (2016) presented a statistical study of 314 SEP events covering the period of 1984 – 2013. They conclude that the majority of the SEP events in their catalogue does not correspond to the two-class classification.

The relationships between SEP events and various types of radio emissions have been widely investigated. Lin (1970) found that 70% of SEP events were associated with type II and type III radio bursts. Kahler (1982) claimed that half of the metric type II events located on the western side of the Sun was accompanied by SEP events. Cane et al. (2002) proposed that the complex type III radio bursts were associated with SEP events. Cliver et al. (2004) suggested that the high energy $\sim$ 20 MeV SEPs are well associated with metric type II bursts that have DH counterparts. Gopalswamy et al. (2005) investigated the connection between SEPs and the type II radio bursts in different wavelengths. They suggest that most of the metric-to-kilometric type II bursts were associated with SEP events. Cliver & Ling (2009) found that the gradual events were associated with type II radio bursts in the DH wavelengths, while the impulsive events had no association in DH type II. Miteva et al. (2013) found that both gradual and impulsive categories of SEP events have highest tendency to be associated with type III radio bursts, and lower tendency with type II. In a recent study Prakash et al. (2017) found that 65% of the metric-to-decahectometric wavelength type II radio bursts associated with CMEs and solar flares produced SEP events.

Chapter 4

PLASMA DENSITY MODELS OF THE SOLAR CORONA

The plasma frequency $[f_p]$ in Hz is directly related to the local electron density $[n_e]$ in cm^{-3} by

$$f = 9000\sqrt{n_e}, \tag{4.1}$$

The electron density can be transformed into atmospheric height by using different atmospheric density models. The most widely used models have been formulated by Newkirk (1961) and Saito (1970). In order to relate the emission frequency to the height in the corona, Newkirk (1961) electron number density at a given heliocentric distance is given by

$$N_e = 4.2 \times 10^4 \times 10^{4.32/R}, \tag{4.2}$$

where R is the distance from the center of the Sun in the units of solar radius ($R_\odot$). In this model, the electron number densities remain high at long distances from the Sun since the model is a hydrostatic one (see Figure 4.1). This model is inconsistent with the model of Mann et al. (1999, 2003), where the density is much larger in the corona than in IP space. This inconsistency arises because the Newkirk model does not take into account the effect of the solar wind. In IP medium the approximation $n_e \propto R^{-2}$ is mostly used and leads to $f_p \sim R^{-1}$. Therefore the plasma density scales as

$$n_e = \frac{n_0}{{R_d}^2}, \tag{4.3}$$

where R_d is the distance from the Sun in AU, and n_0 (cm^{-3}) is the plasma density near Earth at 1 AU. The value of n_0 ranges from $\sim$5 cm^{-3} around solar minimum to ten times this value at solar maximum. The two-fold Newkirk (1961) density model is often used for densities in streamer regions and in active region solar corona.

The Saito (1970) density model is based on white light eclipse observations during the minimum solar activity :

$$N_e = 3.09 \times 10^8 R^{-16} + 1.58 \times 10^8 R^{-6} + 0.0251 \times 10^8 R^{-2.5}, \tag{4.4}$$

The Saito (1970) model is used for equatorial regions in the corona, and at large distances from the Sun, where active region densities no longer dominate. It is often necessary to multiply the density models by a constant value, e.g., two-fold Saito, in order to make them appropriate for describing active regions. Ten-fold Saito can be used when a shock is propagating through high-density loops in the low corona. The model of Saito (1970) was modified by Saito et al.

(1977), where the radial dependence of the density approaches to $n_e \sim R^{-2}$. As the Newkirk model, the saito model gives high densities in the IP space.

Leblanc et al. (1998) model gives densities of low corona and IP space. This model derived the electron density distribution in the ecliptic plane as:

$$N_e = 3.3 \times 10^5 R^{-2} + 4.1 \times 10^6 R^{-4} + 8 \times 10^7 R, \tag{4.5}$$

The model is valid for $R > 1.2$ R$_\odot$ and not valid for $R < 1.2$ R$_\odot$. At large distances $R >$ 30 R$_\odot$ the model is characterised by $n \propto R^{-2}$ and gives an electron density of 7.2 cm^{-3} near 1 AU.

The atmospheric electron density model by Vršnak et al. (2004b), called the hybrid density model, is a model that gives densities of the upper corona and IP space without breaks or discrepancies:

$$N_e = 15.45 \times 10^8 R^{-16} + 3.16 \times 10^8 R^{-6} + 10^8 R^{-4} + 0.0033 \times 10^8 R^{-2}, \tag{4.6}$$

The hybrid model is a mixture of the five-fold model of Saito (1970) and the Leblanc et al. (1998) model, with small modifications. Figure 4.1 demonstrate how the electron density highly depends on coronal conditions.

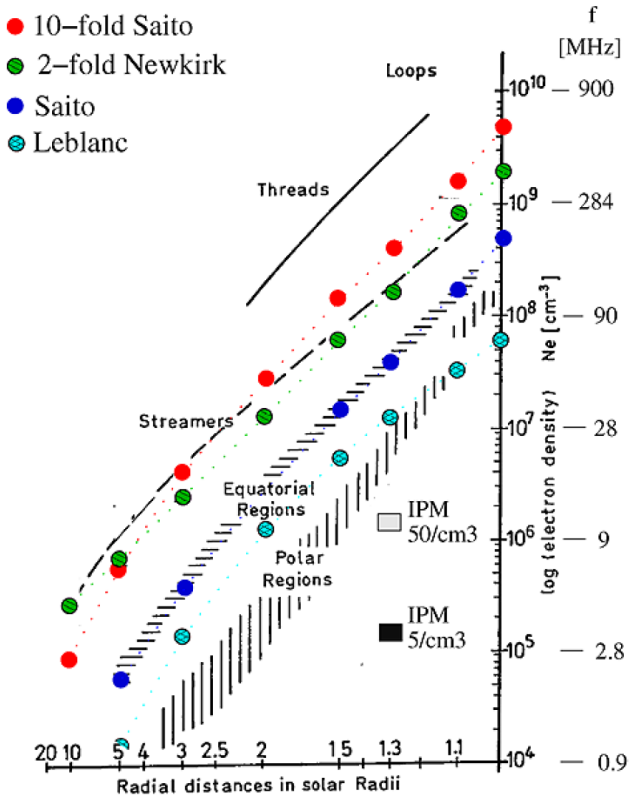

Figure 4.1: Electron density in different parts of the corona from eclipse photometry. Figure from Pohjolainen et al. (2007).

Chapter 5

INSTRUMENTS

5.1 X-rays

5.1.1 Yohkoh SXT

The *Soft X-ray Telescope* (SXT) onboard the Yohkoh (Tsuneta et al., 1991) contains five X-ray analysis filters (Al 0.1 μm, AlMgMn sandwich, Be 119 μm, Al 12, Mg 3 μm) on two rotatable filter wheels located in front of the CCD detector, and provides a pixel-by-pixel temperature diagnostic capability. The filter wheel is controlled by a microprocessor, thus providing very versatile observing sequences. The temperatures and emission measures are obtained from images taken with two different broadband X-ray filters.

Yohkoh/SXT full-disk images were a part of our data analysis in **Paper V**.

5.1.2 RHESSI HXR

The *Reuven Ramaty High-Energy Solar Spectroscopic Imager* (RHESSI) (Lin et al., 2002), is designed to image solar X-rays and gamma rays with high energy resolution. RHESSI spectrometer is able to process up to millions of hard X-rays per second for imaging, while carefully collecting rare gamma-ray line photons with high efficiency, high energy resolution, and without interference from the X-rays. The spectrometer is an array of segmented coaxial germanium detectors. When high purity germanium is at freezing temperatures, no electron-hole pairs are in the conduction band, but a hard X-ray or gamma ray interacting in the crystal will release one or more energetic electrons, which lose energy by creating free pairs. If there is a high electric field across the crystal, the electrons and holes will be pulled to each electrode, creating a current pulse that can be amplified and digitized by suitable electronics. The total charge in the current pulse is proportional to the photon energy.

The Summary plot of GOES/RHESSI HXR/WIND data was a part of our data analysis in **Paper I**.

5.1.3 GOES

The *Geostationary Operational Environmental Satellites* (GOES) observed the Sun and Earth in geosynchronous orbit, with an orbital period the same as the Earth's rotation period. There are two satellites at least operating at the same time to cover 24 hours every day. GOES satellites are operated by *National Oceanic and Atmospheric Administration* (NOAA). The X-ray

telescope with X-ray sensor unit (XRS) is the main instrument onboard GOES, which supply the solar X-ray fluxes at wavelength bands 1–8 Å to 0.5–4 Å.

The solar flare classification is derived from the X-ray spectrometers on the GOES spacecraft (1 – 8 Å band). The classification system for solar flares is using the letters A, B, C, M, and X, according to the peak flux, where the peak fluxes are in the range 10^{-8} to 10^{-4} W m^{-2} at 1 AU from the Sun (see table 2.1).

GOES soft X-ray data were used in the analyses in all papers of this thesis.

5.2 Solar Wind

5.2.1 SOHO/CELIAS

The *Charge, Element, and Isotope Analysis System* (CELIAS) (Hovestadt et al., 1995) onboard SOHO, is designed to study the composition of the solar wind. The CELIAS instrument consists of three mass and charge distinguishing sensors based on the time-of-flight (TOF) technique: charge time-Of-flight (CTOF), mass time-of-flight (MTOF), suprathermal mass time-of-flight (STOF). The MTOF unit sensor was used in this thesis to determine the shock passage associated with the our studied events.

CELIAS measurements of solar wind parameters were used **in Papers I, II, III, and V**.

5.3 Particles

5.3.1 SOHO/ERNE

The *Energetic and Relativistic Nuclei and Electron* (ERNE) experiment (Torsti et al., 1995) onboard SOHO investigates solar atmosphere and heliosphere via detecting particles created in different types of energy release processes. The ERNE telescopes cover the energy range from about 1 MeV/nucleon up to a few hundred MeV/nucleon. It is capable to identifying elements from hydrogen to zinc and to distinguish the most abundant isotopes. ERNE sensor unit contains two detector telescopes, the *Low Energy Detector* (LED) and the *High Energy Detector* (HED).

Low Energy Detector (LED)

LED operates in the low-energy range 1.3 – 13 MeV/n. It consists of two layers of silicon detectors D1 and D2. The anticoincidence detector AC is used to block particles penetrating through the entire sensor. The first detector layer D1 is very thin compared to the D2 layer and consists of seven individual detectors D11 – D17. The cross section view of LED is shown in Figure 5.1.

High Energy Detector (HED)

HED consists of six layers of silicon detectors (S1, S2, D1) and two layers of scintillators (D2, D3) surrounded by anticoincidence shield (AC) as shown in Figure 5.2. The anticoincidence shield rejects particles which do not stop in the upper detector layers. HED detects protons in the energy range 11 – 120 MeV/n and heavier nucleus in the range 11 – 540 MeV/n.

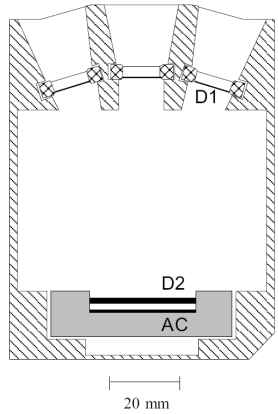

Figure 5.1: Cross section of the low energy detector. Figure from Torsti et al. (1995).

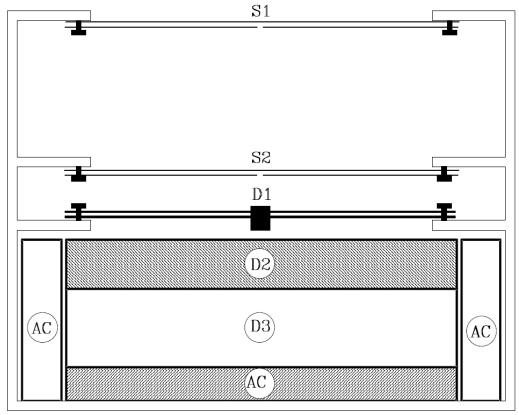

Figure 5.2: Cross section of the high energy detector. Figure from Torsti et al. (1995).

HED has the capability to measure the anisotropy of particles with very high accuracy (Torsti et al., 2004). The HED view cone is divided in 240 small fixed solid angles, 10 concentric rings and 24 azimuthal sectors (see Figure 5.3). This division allows HED to have equal count rates in all pins during isotopic flux conditions.

The energetic proton observations from SOHO/ERNE were used in **Papers I, II, and III**, of this dissertation. The anisotropy index measurements were used in **Paper I**.

5.3.2 SOHO/EPHIN

The *Electron, Proton, and Helium Instrument* (EPHIN) (Müller-Mellin et al., 1995) onboard SOHO is a part of the *Comprehensive Suprathermal and Energetic Particle Analyzer* (COSTEP). The scientific objectives of EPHIN are studies of the steady processes in the solar atmosphere, energy deposition and particle acceleration in the solar atmosphere, the structure of the solar atmosphere, and to understand more about processes in the interplanetary space. EPHIN was designed to measure the energy spectra of electrons from 250 keV to more than 8.7 MeV and of hydrogen and helium isotopes from 4 MeV/n to more than 53 MeV/n. The EPHIN sensor is composed of semiconductor stacks with five layers. They are enclosed by a sixth semiconduc-

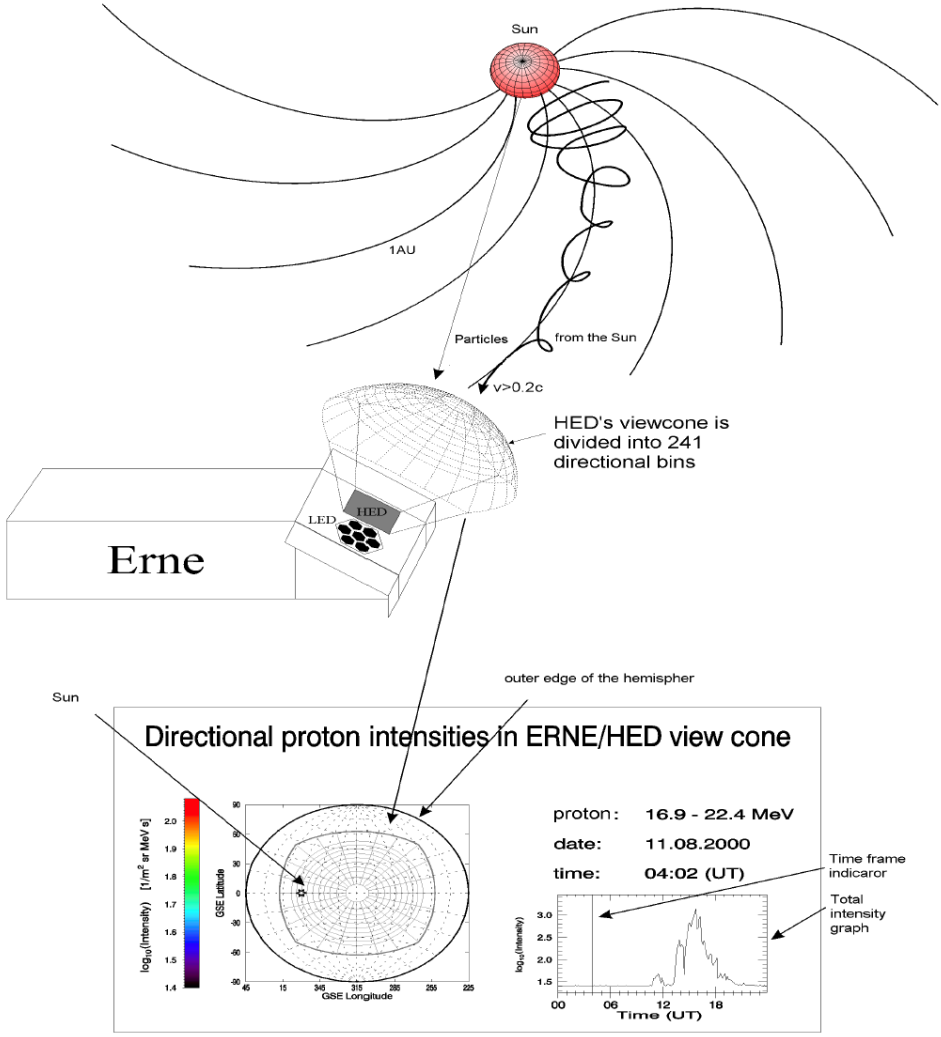

Figure 5.3: Cartoon scenarios for anisotropy measurements by ERNE. Figure retrieved from`https://srl.utu.fi/erne_data/aa/aa.html`

tor detector and a scintillation detector, operated in anticoincidence.

SOHO/EPHIN electron data were used in **Paper III**.

5.3.3 ACE/EPAM

The *Electron, Proton and Alpha Monitor* (EPAM) has been described in full detail by Gold et al. (1998). It is the flight spare of the very successful *Heliospheric Instrument for Spectral Composition and Anisotropy at Low Energies* (HISCALE) (Lanzerotti et al., 1992) onboard the ULYSSES spacecraft, that made the first energetic particle observations over the poles of the Sun (Haggerty et al., 2006). The EPAM instrument is designed to measure electrons and

ions over a wide range of energy and intensity with five separate solid-state detector telescopes that provide nearly full coverage of the unit sphere. The EPAM instrument was selected for the *Advanced Composition Explorer* (ACE) spacecraft (Stone et al., 1998) to observe the low energy (0.046 – 4.8) MeV protons near the Earth's first Lagrangian (L1) point and for its unique capability to measure the near-relativistic (38 – 315) keV electrons (Haggerty et al., 2006).

ACE/EPAM electron data were used in **Paper III**.

5.4 Extreme Ultraviolet

5.4.1 SOHO/EIT

The *Extreme ultraviolet Imaging Telescope* (EIT) (Delaboudinière et al., 1995), is an instrument on the SOHO spacecraft used to obtain high-resolution images of the solar corona in the ultraviolet range. It is designed to supply the entire disk images of the solar transition region and inner solar corona to 1.5 $R_{\odot}$. As well the EIT images provide a critical link between observations of internal and external corona and it also serves to correlate SOHO data with ground-based observations. The EIT instrument is sensitive in four different wavelengths: 17.1 nm observes corona/transition region boundary; 19.5 nm observes quiet corona outside and in coronal holes; 28.4 nm observe active regions; and 30.4 nm observes the chromosphere network (Delaboudinière et al., 1995).

SOHO/EIT images were a part of our data analysis in all papers of this thesis.

5.4.2 STEREO/SECCHI/EUVI

The *Extreme Ultraviolet Imager* (EUVI) (Wuelser et al., 2004), is a part of the *Sun-Earth Connection Coronal and Heliospheric Investigation* (SECCHI) (Howard et al., 2008) instrument suite onboard the *Solar Terrestrial Relations Observatory* (STEREO) (Kaiser et al., 2008) spacecraft. The twin EUVI telescopes on the two STEREO spacecraft investigate the structure and evolution of the solar corona in three dimensions out to 1.7 $R_{\odot}$ and in particular focus on the initiation and early evolution of CMEs . The scientific goals of EUVI include: 1) the initiation of CMEs (interaction of flux system, reconnection), 2) physical evolution of CMEs (3D structure, CME acceleration, and response of low corona), 3) 3D structure of active regions. The EUVI 2048 $\times$ 2048 pixel detectors will have a full Sun field of view, and observes the chromosphere and low corona in four different wavelengths: 17.1 nm, 19.5 nm, 28.4 nm, and 30.4 nm, corresponding to the light produced by highly ionized Fe IX, Fe XII, Fe XV, and He II respectively.

SECCHI/EUVI data were a part of our data analysis in **Paper IV**.

5.5 Radio

5.5.1 Wind/WAVES

The radio and plasma wave investigation on the Wind spacecraft (WAVES) has several sensitive radio receivers that cover the frequency range from $\sim$4 kHz to $\sim$14 MHz (Bougeret et al., 1995), thus providing information on both DH and km type II bursts. The gap from 2 to 20 MHz between ground-based and space-borne observations has been a major obstacle to understanding the relationship between coronal and IP shocks. With WAVES, this gap has

essentially been closed. The receivers are connected to dipole antennas in the spacecraft spin plane and a dipole antenna along the spacecraft spin axis. WAVES detects radio emissions in three different spectral ranges by means of three receivers: Radio Receiver Band 2 (RAD2: 13.825 – 1.075 MHz), Radio Receiver Band 1 (RAD1: 1040 – 20 kHz), and Thermal Noise Receiver (TNR: 245 – 4 kHz). The spectral range of the RAD1 receiver starts in the hectometric range (288.5 m) and ends in the km domain (15 km). The RAD2 spectral range corresponds to 21.7 to 279 m (DH wavelength range).

Wind/WAVES radio dynamic spectrum were a part of our data analysis in all papers of this thesis.

5.5.2 STEREO/WAVES

The STEREO/WAVES experiment (SWAVES) onboard the STEREO spacecraft, is devoted to measure the radio spectrum at frequencies between a few kHz and 16 MHz and follows radio disturbances from the Sun to the Earth (Bougeret et al., 2008). The SWAVES antenna system is a compose of 6 m long orthogonal monopoles intended to measure the electric component of the radio waves.

The STEREO/WAVES consists of a fixed, high frequency receiver (HFR), a low frequency receiver (LFR), and a time domain sampler (TDS).

STEREO/WAVES radio dynamic spectrum were a part of our data analysis in **Paper IV**.

5.6 Hα, White light, and Magnetic Field

5.6.1 Kanzelhöhe Observatory

The Kanzelhöhe observatory (KSO) in Austria, regularly performs high resolution and high cadence imaging of the solar chromosphere in the Hα and Ca II K spectral lines as well as in the solar photosphere in white light. The KSO is operated throughout the year at a mountain ridge in southern Austria near Villach. The site allows solar observations for about 300 days a year, typically 1400 hours of patrol time.

Kanzelhöhe Hα images were used in **Paper V**.

5.6.2 SOHO/LASCO

The *Large Angle and Spectrometric Coronagraph* (LASCO) (Brueckner et al., 1995), is a set of three coronagraphs (C1, C2 and C3) onboard the SOHO satellite located at L1 vantage point. It is able to detect CMEs in white light and observe their propagation over a large distance. The LASCO instrument images the solar corona from 1.1 – 30 $R_\odot$ as follows: LASCO/C1 covers 1.1 – 3.0 $R_\odot$ field-of-view (FOV), LASCO/C2 has a range of 1.5 – 6.0 $R_\odot$, and LASCO/C3 provides white light images beyond C2 FOV in the range of 3.7 – 30 $R_\odot$.

The C1 coronagraph was a newly developed mirror version of the classic internally-occulted Lyot coronagraph (C1 camera was lost in June 1998), while C2 and C3 are externally occulted instruments. The purpose of the occulting coronagraph is to make an artificial eclipse in order to observe faint emissions from the corona in white light.

SOHO/LASCO white light images were a part of our data analysis in all papers of this thesis.

5.6.3 STEREO/SECCHI

COR1 is a classic Lyot internally-occulting refractive coronagraph (Lyot, 1939), adapted for the first time to be used in space. COR1 is designed to detect weak light from the solar corona in the existence of scattered light from the much brighter solar photosphere. The COR1 coronagraphs routinely provide images of the corona at heights from $\sim$1.5 $R_\odot$ to 4 $R_\odot$ where the transition from closed to open coronal structures occur for the first time (Howard et al., 2008). The coronagraph contains a linear polarizer, which is used to inhibit scattered light and to snatch the polarized brightness signal from the solar corona.

COR2 coronagraph images are the most commonly used data for CME analysis between the different kinds of data presented by the STEREO/SECCHI suite of instruments. It is an externally-occulted Lyot coronagraph and derives its legacy from the highly successful LASCO C2 and C3 coronagraphs. Similar to COR1, the coronagraph COR2 is designed to observe the weak coronal signal in visible light. The field of view of COR2 images covers 2.5 – 15 $R_\odot$ (Howard et al., 2008). Images of the white-light CME coronographs COR1 and COR2 are showed in Figure 5.4.

STEREO/SECCHI white light images were a part of our data analysis in **Paper IV**.

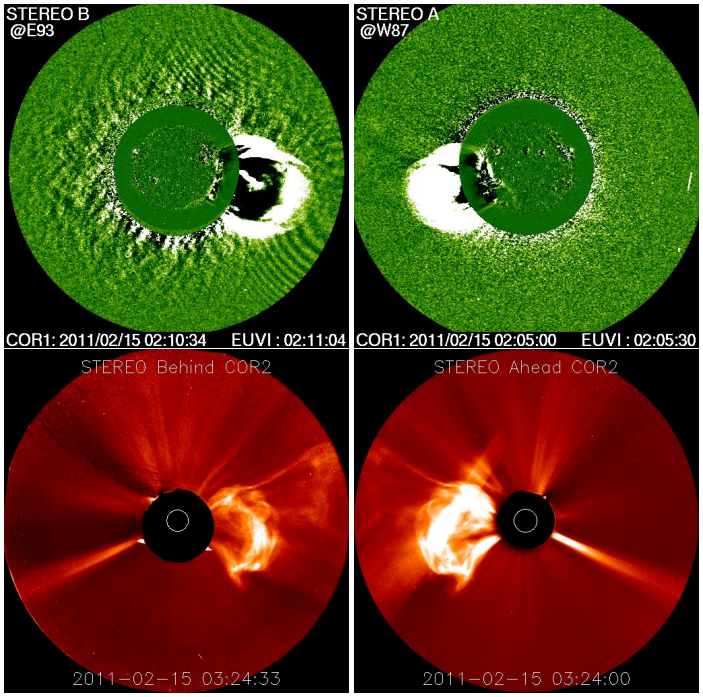

Figure 5.4: The upper panel show the CME on 15 February 2011 observed by COR1 of STEREO B (left) and STEREO A (right). The bottom panel is COR2 images of STEREO B (left) and STEREO A (right) of the same CME.

5.6.4 ACE/MAG

The ACE/*Magnetic Field Experiment* (MAG) is a triaxial, fluxgate magnetometer, with twin sensors (Smith et al., 1998). MAG establishes the time varying, large-scale structure of the

Interplanetary Magnetic Field (IMF) near the L1 point as derived from the continuous measurement of the local field at the spacecraft. On the ground, the MAG data values are collected to produce a 1-min average of the IMF vector. This ground analysis includes de-spinning the measurements and rotating the field into heliocentric radial tangential normal (RTN) and magnetospheric GSM coordinates.

ACE/MAG magnetic filed data were used in **Paper III**.

5.7 ENLIL model

The global 3D MHD Wang-Sheeley-Arge (WSA)-ENLIL+Cone model (hereafter ENLIL) (Odstrcil et al., 2004; Arge et al., 2004), provides a time dependent description of the background solar wind plasma and magnetic field into which a CME can be inserted. ENLIL allows us to insert a CME-like feature at the inner boundary of the ENLIL numerical mesh (21.5 $R_{\odot}$) and tracks the propagation of the solar wind disturbance through the heliosphere (Mays et al., 2015). ENLIL is installed at the *Community Coordinated Modeling Center* (CCMC) and executed in real-time at the CCMC/Space Weather Research Center. The cone model is based on the idea that close to the Sun, CME propagates with constant angular and radial velocity, so that it has the shape of a cone. The model system does not simulate the CME initiation but uses the kinematic properties of CMEs inferred from coronagraphs to launch a CME-like hydrodynamic structure into the solar wind and interplanetary magnetic field computed from the WSA coronal model (Mays et al., 2015).

ENLIL with cone model was used to simulate CMEs in **Paper II**

5.8 SolarSoft

The SolarSoftWare (SSW) is based on collaborative software development that provides a common programming and data analysis environment for solar physics (Freeland and Bentley, 2000). The SSW system has been built using the astronomy and software libraries from many solar satellites, ground-based observatories, data centers, etc., and it draws upon contributions from members of the solar community. The programs are written with the interactive data language (IDL).

Most of the solar data are publicly available and provided by web catalogue interfaces, or they are included in the Solarsoft package. The data are usually given as flexible image transport system (FITS) files, which after downloading can be read into SSW.

The Wind/WAVES dynamic spectra in **Paper III** were done using a SSW-integrated software. The SOHO/EIT difference images in **Paper III** and the SOHO/EIT partial images in **Paper V** were also prepared with SSW programs. The SOHO/MDI magnetogram showing the potential magnetic field lines in **Paper V** were plotted with the SSW potential field source surface (PFSS) program.

Chapter 6

SUMMARY OF THE PUBLICATIONS

6.1 Paper I

Analysis of Multi-Eruption Solar Energetic Particle Events (MESEP) on March 17-18, 2003

In this paper we analyse a series of events with three peaks in the particle intensity-time profiles within a time interval of $\sim$26 hours, observed by SOHO/ERNE and originating from the same active region. We study the particle release time, ^{4}He/proton ratio, and the flux anisotropy in order to distinguish between possible coronal and interplanetary accelerations.

The first event was weak and proton intensity enhancement was observed only below $\sim$25 MeV. The event was associated with an impulsive Hα flare starting at 10:09 UT on March 17 at location S16W33 and with a type III radio burst. There was no CME associated with this flare. The flare was also associated with a hard X-ray emission. Another Hα flare was observed at 11:47 UT associated with hard X-rays. Since accelerated particles are visible in hard X-rays and because type IIIs indicate open field lines, both 10:09 UT and 11:47 UT flares can be possible accelerators of the particles in the first peak.

The second particle event was associated with an X1.5 flare and a fast and wide CME reported to be radio quiet. The X-class flare seems to be long-lasting with thermal emissions and superposed peaks listed as separate flares. The third SEP event occurred about 18 hours later on the tail of the second one, reached proton energies up to $\sim$60 MeV, and lasted for roughly 2 days at energies $>$10 MeV. This event consists of a partial halo CME followed by a radio type II burst in DH wavelength and associated with an X1.5 flare from the same active region.

We estimated the SEP onset time with the help of velocity dispersion analysis (VDA), which makes it possible to infer the release time of particles at the Sun and the apparent path length travelled. The VDA of the first event gave a release time of 10:06 UT $\pm$ 6 minutes, close to the solar flare start. For the second event the VDA release time was 19:00 UT $\pm$ 3 minutes, which is in agreement with the time obtained for the CME liftoff from the linear fit to LASCO observations, while release time of the third event was 12:37 UT $\pm$ 17 minutes. The ratio of ^{4}He/p has been used to identify different classes of SEP events, and it was found to be a good tool also for our study, since different ratios in different peaks indicate contributions of different component to the single event.

We concluded that the first small SEP enhancement was due to flare acceleration. The following two peaks were produced by shock waves driven by fast CMEs.

6.2 Paper II

Observations of Solar Energetic Particle Events During Multiple Coronal Mass Ejections

In this paper we analyse triple flare-CME events originating from the same active regions. The analysed events, on 24 – 26 November 2000, 9 – 13 April 2001, and 22 – 25 August 2005, were all halo CMEs associated with X- or M-class flares.

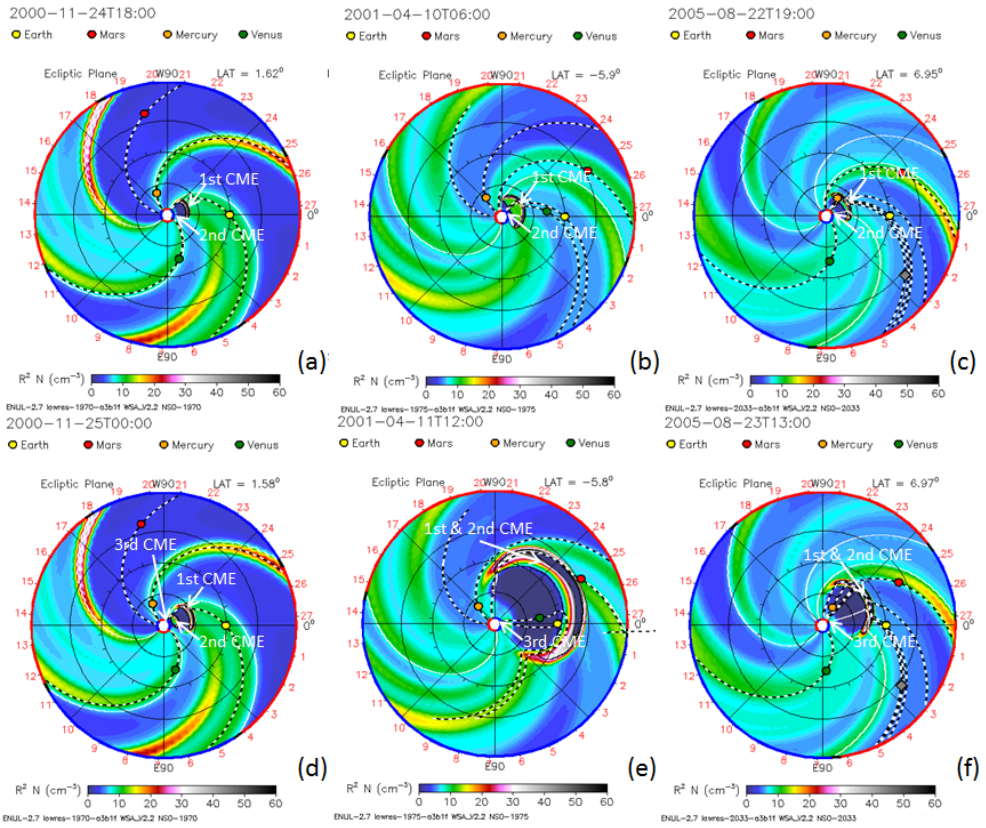

Figure 6.1: Figure 2 of paper II.

The main objective of this study was to discuss how the energetic particles can spread during multiple solar eruptions. Our requirement for the analysed events was that there had to be at least three sequential CMEs that were produced from the same active region within three-four days. Each CME had to be associated with an IP radio type II burst, a sign of a propagating shock wave that is capable of accelerating particles.

To have some evidence of how IP conditions might influence the particle propagation and why only two proton events, associated with the first two flare-CMEs, were observed, we carried out simulations by using the ENLIL with cone model available at the Community Coordinated Modeling Center.

Figure 6.1 (a) shows the plasma density in IP space on 24 November 2000 at the time when the second CME has already been launched, but had not yet reached the inner boundary of the ENLIL simulation (21.5 $R_{\odot}$). At this time the first CME had reached the distance ∼0.3 AU

and protons associated with the second CME had been observed. Obviously, the first CME front ahead of the second CME did not prevent particles reaching the observation point at L1. Figure 6.1(d) presents the conditions 6 hours later after the launch of the third CME. In this case, no particles were observed by SOHO/ERNE. Either the flare/CME processes were unable to accelerate high-energy particles, particles were confined close to the Sun, or were obstructed by the two previous CME fronts from reaching L1.

On 09-11 April 2001 the locations of the CME fronts at the approximate times of the launch of the second and third CME are shown in Figure 6.1 (b) and (e), respectively. At 06:00 UT on April 10, the second CME had been launched (not yet visible in Figure 6.1 (b)) and the first CME front had reached the distance of $\sim$0.3 AU and seems to block the path of particles associated with the second CME to Earth. A clear enhancement of particle intensities was, however, observed. The much faster second CME merged with the first one at $\sim$0.5 AU. When the third CME was launched, the merged CMEs 1 and 2 had already passed the Earth orbit. However, no particles were observed associated with the third flare-CME.

On 22 – 23 August 2005 around the time when the second CME was launched, the first CME was at a distance of $\sim$0.3 AU between the Sun and Earth (Figure 6.1 (c)). Protons associated with the second flare-CME event were, however, clearly observed. About 1 – 2 hours before the third flare-CME event the merged CMEs 1 and 2 were at a distance of $\sim$0.8 AU (Figure 6.1 (f)). This CME/shock front could prevent the access of particles associated with the third flare-CME to near Earth.

In the analysed sequences of events, observed in the years 2000, 2001, and 2005, the first two in-row solar bursts were associated with a SEP enhancement, but the third was not. For the first burst in each sequence the SEP injection time was found to be 0.4-0.7 hours after the flare start, at which time the CME was at a height of about 2.5 – 4.0 $R_{\odot}$. For the second bursts in row, a delay in the SEP injection time was found in two cases (10 April 2001 and 22 August 2005 events). No delay was observed in the 24 November 2000 case. All the events were associated with radio type II and III bursts. However, in each sequence only the first two type III bursts continued down to the plasma frequency level near Earth. In all three sequences the third type III bursts ended at a higher frequency, near 200 kHz (24 November 2000), 60 kHz (11 April 2001), and 50-80 kHz (23 August 2005).

The results from our analysis of the three triple-event sequences suggest that electron beams cannot propagate directly through plasma structures created by at least two earlier CMEs and their associated propagating shocks. The same could be expected for energetic protons. An alternative explanation for not observing SEP enhancement associated with the third in-a-row flare/CME event could be that the earlier CMEs have wiped out most of the seed particles, with no particles left for the third CME to accelerate.

6.3 Paper III

Propagation of Solar Energetic Particles During Multiple Coronal Mass Ejection Events

In this paper we investigate the same events as in paper II, but using different data sets. The preliminary candidate list consisted of 17 sequences of consecutive events. Our basic selection criteria for the analysed events were that there had to be at least three consecutive CMEs that originated from the same active region within three-four days and that each of the CMEs was associated with an IP radio type II burst. Further requirements were that the CMEs had to be separable from each other so that their associated features could be investigated and that

energetic protons associated with the first two CMEs were observed. Data gaps in the in situ particle data made the analysis impossible for some events. Eventually, three triple-events remained for analysis.

The aim of this study was to analyse triple events where the first two CMEs are associated with SEP enhancements, but at the time of the third CME no SEP enhancement is observed. We use solar radio data and in-situ magnetic field measurements to investigate how particle beams and shock fronts propagate during these time periods, to determine whether the particle propagation conditions or acceleration processes change in the course of the successive events.

The selected events, on 24 November 2000, 9 – 11 April 2001, and 22 – 23 August 2005, were all halo CMEs originating from the same active regions and were associated with X-or M-class flares. In all cases clear EUV waves, type III bursts, and IP type II radio emissions were observed, indicative that the CMEs were driving IP shocks. The first two CMEs and flares in each group of the triple eruptions were associated with large SEP events up to high ($\sim$100 MeV) proton energies, while the third one in each case was not associated with an observable enhancement of proton intensity. We investigated the possible solar and IP causes for the absence of solar protons at $\sim$1 AU during the third in row eruptions.

On 24 November 2000 three GOES X-class flares and halo CMEs associated with IP type II radio bursts were observed to originate from the same active region NOAA 9236. The first IP type II burst was rather complex in the beginning of the burst, but it was very intense, with a clear narrow-band emission lane at frequencies below 1 MHz. The second type II burst was comprised of narrow-band short-duration bursts, with a separate, more diffuse emission lane at lower frequencies. The third type II burst was visible only down to 3 MHz. We compared the observed CME heights with the shock heights by calculating the radio source heights for the observed IP type II bursts. All three flare-CME events were also associated with radio type III bursts. The first two continued down to the plasma density level near Earth, to about 30 kHz, but the third one ended at about 200 kHz. This plasma frequency corresponds in standard solar atmospheric density to a distance of about 30 $R_\odot$ from the Sun centre.

On 09 – 11 April 2001 three consecutive CME-and IP type II burst-associated flares were launched from the active region NOAA 9415. The radio spectrum revealed a short-duration IP type II burst at 12 – 7 MHz on 9 April with intermittent emission at lower frequencies. The second IP type II burst on 10 April had a very wide and diffuse emission band. The third IP type II burst on 11 April had a narrow band and it was visible for less than two hours from the beginning of the flare-CME event. The calculated source heights of the first type II burst were in good agreement with the heights of the associated CME. All three flare-CME events were associated with radio type III bursts. The first two type IIIs continued down to the plasma density level near Earth, to about 30 kHz, but the third ended near 60 kHz. In standard atmospheric density this corresponds to a distance of about 90 $R_\odot$ from the Sun centre.

On 22 – 23 August 2005 three consecutive M-class flares from the active region NOAA 10798 associated with halo CMEs were observed. All three flare-CME events were also associated with an IP type II burst. The first IP type II burst on 22 August had a strong, narrow emission lane which could be followed from 2 MHz down to 400 kHz. The next type II burst on the same day was more chaotic, with patches of emission superposed on weaker emission. The third type II burst on 23 August showed very clear and narrow emission bands both at the fundamental and harmonic plasma frequencies. The calculated type II burst source heights were in good agreement with the CME heights of the first and second CME. The calculated type II heights associated with the third CME were considerably lower than the estimated CME heights after the event start, similar to the wide-band type II shock on 10 April 2001. The type III bursts associated with the two first flare-CMEs continued down to the plasma density level

near Earth, to about 30 kHz, but the third ended near 50 – 80 kHz.

The velocity dispersion analysis of the particles associated with the first burst in each sequence gave a solar proton injection time of 0.4 – 0.7 hours after the flare start, at which time the CME was at a height of about 2.5 – 4.0 $R_\odot$. For the second bursts in the row, a delay in the SEP injection time was found in two cases (10 April 2001 and the 22 August 2005 events). The energetic particles could have been injected some 1.6 – 1.7 hours after the flare, when the CMEs were at heights of about 16.0 – 19.0 $R_\odot$. No delay was observed in the 24 November 2000 case. The second SEP injection occurred 0.6 hours after the flare start, at which time the CME was at a height of about 3.0 $R_\odot$.

To explain the missing third SEP event in each sequence, we suggest that the earlier-launched CMEs and the CME-driven shocks either reduced the seed particle population and thus led to inefficient particle acceleration, or that the earlier-launched CMEs and shocks changed the propagation paths or prevented the propagation of both the electron beams and SEPs, so that they were not detected near Earth even though the shock arrivals were recorded.

6.4 Paper IV

Origin of Radio Enhancements in Type II Bursts in the Outer Corona

In this paper we study the enhanced type II radio bursts in the outer corona during the time range 2011 – 2014. The selected period allowed us to get a 3D-view of the events, with the good data coverage from SOHO, Wind, and the two STEREO spacecraft on the opposite sides of the Sun. The aim of this paper was to study CME events that showed enhanced radio emission on top of typical type II burst emission. The event selection was based on the radio enhancement signatures that were identified in the radio dynamic spectra at DH wavelengths. Then we compared the radio data to CME imaging data, to find possible causes for the enhanced emission. We analysed the radio spectral data and the white-light coronagraph data for 16 selected events, to obtain directions and heights for the propagating CMEs and the type II bursts.

Based on our analysis, we found that the radio enhancements can be divided into five different categories depending on their origin:

I. Events where the type II heights agree with the CME heights, indicating that the shock is located at the leading front of the CME. The radio enhancements are superposed on the type II lanes and are probably due to irregularities in the solar wind, i.e., the shock meets remnant material from earlier CMEs but continues to propagate at the same speed.

II. Events where the type II heights agree with the CME leading front heights, within the estimated error margins. The radio enhancements appear at a time when the later CME reaches heights that are 1.5 – 7.5 $R_\odot$ lower than the heights of the earlier CME, or soon after reaching the same heights. This suggests interaction/ merging of the CMEs. In some of these cases frequency/density jumps are observed in the radio spectra.

III. Events where the type II heights are significantly lower than the CME heights almost from the start, and the separation in height grows in time. It is possible that in these cases the shock is located somewhere lower than the CME leading front. From the LASCO and SECCHI images it can be seen that in most of these cases the earlier CMEs did not seem to be at sufficiently low height or dense enough to be causing excess densities. In some cases CME merging, if any, would have already happened when the radio enhancements appeared. In all of these cases there were streamers within the direction of the CME/shock

propagation, suggesting that CME flank-streamer interaction could have been the cause for the enhanced radio emission.

IV. Events where the radio enhancements are located within wide-band type II burst emission.

V. Events where the radio enhancements occur when later-accelerated particles, observed as type III bursts, stop near the type II burst frequency. Enhanced emission could be created when the particle beams meet the CME or shock front and get trapped in the magnetic field. Or the enhanced emission could be due to observing the two different emissions on top of each other.

The drift rates or the bandwidth characteristics or cross-correlations of various characteristics did not reveal any clear association to particular category types. Our conclusion is that the enhanced radio emission, observed during IP type II bursts and associated with CMEs and propagating shocks, can have different origins. We found that CME–CME interaction was the most probable cause in 25 % of the events, but in most cases (38 %), CME flank–streamer interaction looks more probable. The type II emission may also originate either from a CME bow shock or a CME flank shock, which affects the configuration in relation to streamers. Some more unusual events were also found (wide-band enhancements, type III-burst related enhancements), but these remain less clear because of the small number of events.

6.5 Paper V

Formation of Radio Type II Bursts During a Multiple Coronal Mass Ejection Event

In this paper we have analysed radio emission that was associated with three successive CMEs, launched from the same active region within a short period of time on 27 September 2001. The CMEs were associated with low-intensity solar flares and strong type II radio emission at DH wavelengths. The aim of this study is to analyse the radio emission and its association with the CMEs, and to discuss the role of CME interaction during the propagation of different CME structures.

The Wind WAVES experiment observed IP type II bursts after the third flare-CME event. Several separate periods of type II bursts were recorded, the most intense ones appearing at 08:22 – 08:40 UT, 10:40 – 11:15 UT, 11:50 – 13:25 UT, and 14:00 – 17:20 UT.

CME1 had a typical CME structure with a bright front followed by a cavity and a bright core. It was first observed in the field of view of the SOHO/LASCO C2 coronagraph at 01:32 UT at height 3.35 $R_\odot$. We measured the CME1 leading front heights as function of time at position angle 212 degrees, where it was visible up to the height of $\sim$16 $R_\odot$. We also measured the heights of the CME1 core as function of time at the position angle 200 degrees. The first measurement was done at 02:06 UT at height 2.8 $R_\odot$, and the last measurement at 14:42 UT at height $\sim$30 $R_\odot$.

CME2 was observed at 05:06 UT at height 3.1 $R_\odot$ in position angle 243 degrees propagating roughly toward the south-west. CME2 also had a leading front followed by a core. The leading front was only weakly visible and disappeared already at height 5.6 $R_\odot$ at 06:54 UT. We followed the CME2 core at position angle 237 degrees from the height of 3.3 $R_\odot$ at 05:54 UT up to the height of 31.3 $R_\odot$ at 15:42 UT. However, already at 10:20 UT the CME1 core and the core of CME2 had partly merged together forming a bright front surrounding (in the plane of the sky) the third CME, which was apparently pushing the previous two forward. We

measured the heights of CME3 at position angle 212 degrees, i.e., the same angle as the leading front of CME1. Our first measurement was at 08:54 UT at height 4.1 $R_\odot$ and the CME was followed up to the height of > 30 $R_\odot$.

The first IP type II burst appeared at 08:22 UT and the emission covered the frequencies 2.40 – 1.45 MHz. The emission peak frequency of the center lane was 1.875 MHz at 08:22 UT near the start of the burst, which corresponds to a density of 4.3×10^4 cm^{-3}. At 08:37 UT, near the end of this emission lane, the peak frequency was 1.73 MHz, which gives a low burst speed from the frequency drift and suggests that the shock was not propagating along the density gradient.

The second type II burst was identified near 2 MHz at 10:04 UT. This emission was relatively faint and had a narrow bandwidth. Three periods of more enhanced emission occurred after 10:40 UT. The first two enhanced emission lanes look to have similar drift rates. The third enhancement occurred at slightly higher frequencies and had a larger bandwidth.

We conclude that the first radio type II burst could be due to a shock wave launched by sudden acceleration of the CME2 core and accelerating CME3, if the plasma densities were very low ahead of the CMEs, or by accelerating CME1 core if the plasma densities were very high inside the CME1 cavity. The start of the second type II burst at higher frequencies indicates that it was due to a separate shock, propagating to a different direction, within different atmospheric density. Our estimates of the radio source heights suggest that it could also have been a shock at the flanks of either CME2 or CME3. As the CME3 heights were approaching the heights of CME2 (both observed in projection), CME-CME interaction was most probably present and hence the type II emission showed an increased frequency range in the later stages of emission.

As the CME3 heights were approaching the heights of CME2 (both observed in projection), CME–CME interaction was most probably present, and hence the type II emission showed an increased frequency range in the later stages of emission. Sporadic enhancements can be caused by irregularities in the solar wind, like plasma from the earlier transients.

Chapter 7

CONCLUSIONS

In this thesis we have studied the occurrence of solar energetic particle events and the possible source regions of type II radio bursts during multiple coronal mass ejections. To achieve these goals we present analyses of multiwavelength observations of the solar eruptions.

We have shown that energetic particles in events following each other in rapid succession can have different origins. Such multi-eruption events can have particle components which have been accelerated in processes related to the solar flare, as well as components which have been later accelerated in CME-driven shocks in the solar corona or in the interplanetary space. Distinguishing these components from each other requires, in addition to a careful determination of the particle release times from their sources, also measurements of the relative abundances of certain particle species, like the time behaviour of the ^{4}He/proton ratio.

We also investigated the propagation of energetic particles during three sequences of triple flare and CME events originating from the same active region. Whereas only the first two events in each sequence were associated with SEP enhancements near Earth, there was no SEP enhancement observed with the third CME. One explanation for this observation is that the earlier CMEs had wiped out most of the seed particles, with very few particles left for the third CME to accelerate. Other explanations are that the propagation paths of both electron beams and SEPs were changed by the effect of the previous eruptions, or that at some point of their propagation between the Sun and Earth the particles encountered disturbed magnetic fields preventing their propagation to Earth.

Different scenarios on how enhanced radio signatures can be created in the outer corona were discussed. CME–CME interactions were found to be one probable cause, but in most cases CME flank–streamer interactions look more probable. Type II radio emission may also originate either from a CME bow shock propagating through variable plasma structures causing the radio enhancements, or from a CME flank shock which affects the configuration in relation to streamers.

We found several possibilities for the formation of type II radio bursts in a complex event with multiple CMEs. Various structures of CMEs and the relative development of multiple CME propagations play a role in the production of the radio emission. Not only the CME fronts but also the behaviour of the CME cores and possible formation of shocks in the flanks of the CMEs are important. Furthermore, it is evident that a sudden acceleration of CME structures behind earlier CMEs propagating in the interplanetary space can cause interactions of the plasma clouds leading to shock formation and enhanced radio emission with different starting frequencies and frequency time drifts.

Bibliography

Antiochos, S. K.: 1998, *ApJ*, **502**, L181

Antiochos, S. K, DeVore, C. R., Klimchuk, J. A.: 1999, *ApJ*, **510**, 485

Arge, C. N., Luhmann, J. G., Odstrcil, D., Schrijver, C. J., Li, Y.: 2004, *J. Atmosph. Solar-Terrestrial Phys.*, **66**, 1295

Bale, S. D., Reiner, M. J., Bougeret, J. L., et al.: 1999, *JGR*, **26**, 1573

Bastian, T. S., Pick, M., Kerdraon, A., Maia, D., Vourlidas, A.: 2001, *ApJ*, **558**, L65

Bastian, T. S .: 2007, *ApJ*, **665**, 805

Benz, A. O., Magun, A., Stehling, W., Su, H.: 1992, *Sol. Phys.*, **141**, 335

Bougeret, J. L.: 1985, in: Collisionless shocks in the heliosphere, (eds.) B.T. Tsurutani, R.G. Stone, *AGU*, Geophys. Monograph Ser. **35**, 13

Bougeret, J. L. Kaiser, M. L., Kellogg, P. J., et al.: 1995, *Space Sci. Rev.*, **71**. 231

Bougeret, J. L., Goetz, K., Kaiser, M. L., et al.: 2008, *Space Sci. Rev.*, **136**. 487

Brueckner, G. E., Howard, R. A., Koomen, M. J., Korendyke, C. M., et al.: 1995, *Sol. Phys.*, **162**, 357

Burlaga, L. F., Plunkett, S. P., St. Cyr, O. C.: 2002, *JGR*, **107**, 1266

Cairns, I. H.: 1987, *Geophys. Res. Lett.*, **92**, 2315

Cairns, I. H., Robinson, P. A., Anderson, R. P .: 2000, *Geophys. Res. Lett.*, **27**, 61

Cairns,I. H., Knock, S. A., Robinson, P. A., Kunic, Z.: 2003, *Space Sci. Rev.*, **107**, 27

Cane, H. V., Sheeley, Jr., N. R., Howard, R. A.: 1987, *JGR*, **92**, 9869

Cane, H. V., Erickson, W. C., Prestage, N. P.: 2002, *JGR*, **107**, 1315

Cane, H. V., Mewaldt, R. A., Cohen, C. M. S., von Rosenvinge, T. T.: 2006, *JGR*, **111**, A06S90

Carmichael, H.: 1964, Proc. of AAS-NASA Symp. on the Physics of Solar Flares, (ed.) W. N. Hess, **NASA-SP 50**, 451

Carrington, R. C.: 1859, *Mon. Not. Roy. Astron. Soc.*, **20**, 13

Chen, Y.: 2013, *Chin. Sci. Bull.*, **58**, 1599

Chen, Y., Song, H. Q., Li, B., Xia, L. D., Wu, Z., Fu, H., Li, X.: 2010, *ApJ*, **417**, 644

Chen, Y., Feng, S. W., Li, B., Song, H. Q., Xia, L. D., Kong, X. L., Li, X.: 2011, *ApJ*, **728**, 147

Chen, Y., Du, G., Feng, L,. Feng, S., Kong, X., Guo, F., Wang, B., Li, G.: 2014, *ApJ*, **787**, 59

Cho, K. S., Lee, J., Moon, Y. J., Dryer, M., Bong, S. C., Kim, Y. H., Park, Y. D.: 2007, *A&A*, **461**, 1121

Cho, K. S., Bong, S. C., Moon, Y. J., Shanmugaraju, A., Kwon, R. Y., Park, Y. D.: 2011, *A&A*, **530**, A16

Cliver, E. W.: 1996, in AIP Conf. Proc. 374, High Energy Solar Physics, (eds.) R. Ramaty, N. Mandzhavidze, X. M. Hua (Melville, NY: AIP), 45

Cliver, E. W., Webb, D. F., Howard, R. A.: 1999, *Sol. Phys.*, **187**, 89

Cliver, E. W., Kahler, S. W., Reames, D. V.: 2004, *ApJ*, **605**, 902

Cliver, E. W., Ling, A. G.: 2009, *ApJ*, **690**, 598

Delaboudinière, J. P., Artzner, G. E., Brunaud, J., et al.: 1995, *Sol. Phys.*, **162**, 291

Dennis,B. R.: 1988, *Sol. Phys.*, **118**, 49

Desai, M., Giacalone, J.: 2016, *Living Rev. Sol. Phys.*, **13**, 3

Doschek, G. A.: 1990, *ApJ*, **73**, 117

Fainberg, J. Stone, R. G.: 1970, *Sol. Phys.*, **15**, 433

Feng, S. W., Chen, Y., Li, B., Song, H. Q., Kong, X. L., Xia, L. D., Feng, X. S.: 2011, *Sol. Phys.*, **272**, 119

Filbert, P. C. and Kellogg, P. J.: 1979, *JGR*, **84**, 1369

Foukal, P., Miller, P., Gilliam, L .: 1983, *Sol. Phys.*, **83**, 83

Freeland, S., Bentley, R.: 2000, SolarSoft. in: Murdin, P. (ed.) Encyclopedia of Astronomy and Astrophysics, article 3390

Gallagher, P. T., Lawrence, G. R., Dennis, B. R .: 2003, *ApJ*, **588**, L53

Gold, R. E., Krimigis, S. M., Hawkins, S. E., et al.: 1998, *Space Sci. Rev.*, **86**, 541

Gopalswamy, N., Kaiser, M. L., Lepping, R. P., et al.: 1998, *JGR*, **103**, 307

Gopalswamy, N., Kaiser, M. L., Thompson, B. J., et al.: 2000, *Geophys. Res. Lett.*, **27**, 1427

Gopalswamy, N., Yashiro, S., Kaiser, M. L., Howard, R. A., Bougeret, J. L.: 2001a, *JGR*, **106**, 29219

Gopalswamy, N., Yashiro, S., Kaiser, M. L., Howard, R. A., Bougeret, J. L.: 2001b, *ApJ*, **548**, L91

Gopalswamy, N., Yashiro, S., Kaiser, M. L., Howard, R. A., Bougeret, J. L.: 2002a, *Geophys. Res. Lett.*, **29**, 1265

Gopalswamy, N., Yashiro, S., Michałek, G., et al.: 2002b, *ApJ*, **572**, L103

Gopalswamy, N.: 2003, *Geophys. Res. Lett.*, **30**, 8013

Gopalswamy, N., Yashiro, S., Krucker, S., Stenborg, G., Howard, R. A.: 2004, *JGR*, **109**, A12105

Gopalswamy, N., Aguilar-Rodriguez, E., Yashiro, S., Nunes, S., Kaiser, M. L., Howard, R. A.: 2005, *JGR*, **110**, A12S07

Gopalswamy, N., Yashiro, S., Xie, H., Akiyama, S., et al.: 2008, *ApJ*, **674**, 560

Gopalswamy, N.: 2010, Coronal mass ejections: A summary of recent results, (ed.) I. Dorotovic, proceeding of the 20th National Solar Physics Meeting, 108

Gopalswamy, N., Xie, H., Mäkelä, P., Yashiro, S., Kaiser, M. L., Howard, R. A., Bougeret, J. L .: 2010, *ApJ*, **710**, 1111

Gopalswamy, N.: 2011, Coronal mass ejections and their heliospheric consequences, (eds.) A. G. Choudhuri, D. Dipankar Banerjee, First Asia-Pacific Solar Physics Meeting, *Astron. Soc. India.,* **CS-2**, 241

Gosling, J. T., Hildner, E., MacQueen, R. M., Munro, R. H., Poland, A. I., Ross, C. L .: 1974, *JGR*, **79**, 4581

Gronenschild, E. H. B. M., Mewe, R.: 1978, *Astron. Astrophys. Suppl.*, **32**, 283

Habbal, S. R., Woo, R., Fineschi, S., O'Neal, R., Kohl, J., Noci, G., Korendyke, C .: 1997, *ApJ*, **489**, L103

Haggerty, D. K., Roelof, E. C., Ho, G. C., Gold, R. E .: 2006, *Adv. Space Res.*, **83**, 995

Hale, G. E.: 1931, *ApJ*, **73**, 379

Hillaris, A, Bouratzis, C. Nindos, A.: 2016, *Sol. Phys.*, **291**, 2049

Hirayama, T.: 1974, *Sol. Phys.*, **34**, 323

Holman, G. D. Sui, L. Dennis, B. R.: 2006, *American Astronomical Society*, **38**, 243

Howard, R. A., Sheeley, Jr., N. R., Michels, D. J., Koomen, M. J.: 1985, *JGR*, **90**, 8173

Hovestadt, D., Hilchenbach, M., Bürgi., et al.: 1995, *Sol. Phys.*, **162**, 441

Howard, R. A., Michels, D. J., Sheeley, Jr., N. R., Koomen, M. J.: 1982, *ApJ*, **263**, L101

Howard, R. A., Moses, J. D., Vourlidas, A., Newmark, J. S., Socker, D. G., et al.: 2008, *Space Sci. Rev.*, **136**,67

Hudson, H., Haisch, B., Strong, K. T.: 1995, *JGR*, **100**, 3473

Hundhausen, A. J., Sawyer, C. B., House, L., Illing, R. M. E., Wagner, W. J.: 1984, *JGR*, **89**, 2639

Hundhausen, A. J.: 1993, *JGR*, **98**, 13177

Ichimoto, K., Hirayama, T., Yamaguchi, A., et al .: 1992, *Astron. Soc. Japan.*, **44**, L117

Illing, R. M. E., Hundhausen, A. J.: 1983, *JGR*, **88**, 10210

Kahler, S. W.: 1992, *Annu. Rev. Astron. Astrophys.*, **30**, 113

Kahler, S. W.: 1982, *ApJ*, **261**, 710

Kaiser, M. L., Reiner, M. J., Gopalswamy, N., Howard, R. A., St. Cyr, O. C., Thompson, B. J., Bougeret, J. L.: 1998, *Geophys. Res. Lett.*, **25**, 2501

Kaiser, M. L., Kucera, T. A., Davila, J. M., St. Cyr, O. C., Guhathakurta, M., Christian, E.: 2008, *Space Sci. Rev.*, **136**, 5

Kim, Y. H., Bong, S. C., Park, Y. D., Cho, K. S., Moon, Y. J.: 2009, *ApJ*, **705**, 1721

Klassen, A., Aurass, H., Klein, K. L., Hofmann, A., Mann, G.: 1999, *A&A*, **343**, 287

Klassen, A., Pohjolainen, S.: 2002, in Solar Variability: From Core to Outer Frontiers, (ed.) A. Wilson, ESTEC, Noordwijk, The Netherlands, **ESA–SP 506**, 307

Knock, S. A., Cairns, I. H., Robinson, P. A. Kuncic, Z.: 2001, *JGR*, **106**, 25041

Knock, S. A., Cairns, I. H., Robinson, P. A. Kuncic, Z.: 2003, *JGR*, **108**, 1126

Kocharov, L., Torsti, J.: 2002, *Sol. Phys.*, **207**, 149

Kong, X. L., Chen, Y., Li, G., Feng, S. W., Song, H. Q., Guo, F., Jiao, F. R.: 2012, *ApJ*, **750**, 158

Kopp, R. A., Pneuman, G. W.: 1976, *Sol. Phys.*, **50**, 85

Krall, J., Chen, J., Santoro, R.: 2000, *ApJ*, **539**, 964

Kuncic, Z., Cairns, I. H. Knock, S. A.: 2002a, *JGR*, **107**, A8

Kuncic, Z., Cairns, I. H. Knock, S. A.: 2002b, *Geophys. Res. Lett.*, **29**, 47

Kwon, R. Y., Kramar, M., Wang, T., Ofman, L., Davila, J. M., Chae, J., Zhang, J .: 2013, *ApJ*, **776**, 55

Lang,K. R.: 1995, Sun, Earth, and sky, Springer: Berlin

Lanzerotti, L. J., Gold, R. E., Anderson, K. A., et al .: 1992, *A&A.*, **92**, 349

Landini, M., Monsignori Fossi, B. C .: 1990, *Astron. Astrophys. Suppl.*, **82**, 229

Lara, A., Gopalswamy, N., Nunes, S., Muñoz, G., Yashiro, S.: 2003, *Geophys. Res. Lett.*, **30**, 8016

Leblanc, Y., Dulk, G. A., Bougeret, J. L.: 1998, *Sol. Phys.*, **183**, 165

Lin, R. P.: 1970, *Sol. Phys.*, **12**, 266

Lin, R. P, Dennis, B. R., Hurford, G. J., et al.: 2002, *Sol. Phys.*, **210**, 3

Liu, C., Deng, N. Lee, J. Wiegelmann, T. Moore, R. L. Wang, H.: 2013, *ApJ*, **778**, L36

Lyot, B.: 1939, *Mon. Not. R. Astron. Soc.*, **99**, 580

MacQueen, R. M., Eddy, J. A., Gosling, J. T., et al.: 1974, *ApJ*, **187**, L85

Magara, T., Mineshige, S., Yokoyama, T., Shibata, K.: 1996, *ApJ*, **466**, 1054

Mann, G., Jansen, F., MacDowall, R. J., Kaiser, M. L., Stone, R. G.: 1999, *A&A*, **348**, 614

Mann, G., Klassen, A., Aurass, H., Classen, H. T.: 2003, *A&A*, **400**, 329

Maričić, D., Vršnak, B., Dumbović, M., Žic, T., et al.: 2014, *Sol. Phys.*, **289**, 351

Martínez Oliveros, J. C., Raftery, C.L., Bain, H. M., Liu, Y., Krupar, V., Bale, S., Krucker, S.: 2012, *ApJ*, **748**, 66

Mays, M. L., Taktakishvili, A., Pulkkinen, A., MacNeice, P. J., et al.: 2015, *Solar Phys.*, **290**, 1775

Melrose, D. B.: 1980, *Space Sci. Rev.*, **26**, 3

Mercier, C., Elgaroy, O., Tlamicha, A., Zlobec, P.: 1984, *Solar Phys.*, **92**, 375

Michalek, G.: 2009, *A&A*, **494**, 263

Miller, J. A.: 1998, *Space Sci. Rev.*, **86**, 79

Miteva, R., Klein, K. L., Samwel, S. W., Nindos, A., Kouloumvakos, A., Reid, H.: 2013, *Central European Astrophys. Bull.*, **37**, 541

Moon, Y. J., Choe, G. S., Wang, H., Park, Y. D., Gopalswamy, N., Yang, G., Yashiro, S.: 2002, *ApJ*, **581**, 694

Moore, R. L., Sterling, A. C., Hudson, H. S., Lemen, J. R.: 2001, *ApJ*, **552**, 833

Müller-Mellin, R., Kunow, H., Fleißner, V.,Pehlke, E., et al.: 1995, *Sol. Phys.*, **162**, 483

Munro, R. H., Gosling, J. T., Hildner, E., MacQueen, R. M., Poland, A. I., Ross, C. L.: 1979, *Sol. Phys.*, **61**, 201

Nelson, G. J., Robinson, R. D.: 1975, *Proc. Astron. Soc. Australia.*, **2**, 370

Nelson, G. J., Melrose, D. B.: 1985, Solar Radiophysics: Studies of Emission from the Sun at Metre Wavelengths, (eds.) D. J. McLean, N. R. Labrum, (Cambridge, New York: Cambridge Uni. Press), 333

Newkirk, G. Jr.: 1961, *ApJ*, **133**, 983

Odstrcil, D., Riley, P., Zhao, X. P.: 2004, *JGR*, **109**, A02116

Papaioannou, A., Sandberg, I., Anastasiadis, A., et al.: 2016, *J. Space Weather Space Clim.*, **6**, A42

Parker, E. N.: 1961, *ApJ*, **133**, 1014

Pohjolainen, S., van Driel-Gesztelyi, L., Culhane, J. L., Manoharan, P. K., Elliott, H. A.: 2007, *Sol. Phys.*, **244**, 167

Pohjolainen, S., Allawi, H., Valtonen, E.: 2013, *A&A*, **558**, 7

Prakash, O., Feng, L., Michalek, G., Gan, W., Lu, L., Shanmugaraju, A., Umapathy, S.: 2017, *Astrophys. Space Sci*., **362**, 56

Priest, E. R.: 1982, Solar magneto-hydrodynamics, D. Reidel Publ. Comp., Dordrecht

Priest, E. R., Forbes, T. G.: 2002, *A&A,* **10**, 313

Ramaty, R., Murphy, R. J.: 1987, *Space Sci. Rev.*, **45**, 213

Ramesh, R., Kishore, P., Mulay, S. M., Barve, I. V., Kathiravan, C., Wang, T. J.: 2013, *ApJ*, **778**, 30

Reames, D. V.: 1990, *ApJ*, **73**, 235

Reames, D. V., Meyer, J. P., von Rosenvinge, T. T.: 1994, *ApJ*, **90**, 649

Reames, D. V.: 1999, *Space Sci. Rev.*, **90**, 413

Reames, D. V.: 2002, *ApJ*, **571**, L63

Reames, D. V.: 2013, *Space Sci. Rev.*, **175**, 53

Reid, H. A. S., Ratcliffe, H.: 2014, *Res. Astron. Astrophys.*, **14**, 773

Reiner, M. J., Kaiser, M. L., Fainberg, J., Bougeret, J. L., Stone, R. G.: 1997, Remote radio tracking of interplanetary CMEs, (ed.) A. Wilson Correlated Phenomena at the Sun, Noordwijk, **ESA-SP 415**, 183

Reiner, M. J., Kaiser, M. L., Fainberg, J., Bougeret, J. L., Stone, R. G.: 1998a, *Geophys. Res. Lett.*, **25**,2493

Reiner, M. J., Kaiser, M. L., Fainberg, J., Stone, R. G.: 1998b, *JGR*, **103**,29651

Reiner, M. J., Kaiser, M. L., Gopalswamy, N., et al.: 2001, *JGR*, **106**, 25279

Reiner, M. J., Vourlidas, A., Cyr, O. C. S., et al.: 2003, *ApJ*, **590**,533

Richardson, R. S.: 1951, *ApJ*, **114**, 356

Robinson, R.D., Sheridan, K. V.: 1982, *Publ. Astron. Soc. Pac.*, **4**, 392

Robinson, R.D., Cairns, I. H., Willes, A. J.: 1994, *ApJ*, **422**, 790

Saito, K.: 1970, *Ann. Tokyo Astron. Obs.*, **12**, 53

Saito, K., Poland, A. I., Munro, R. H.: 1977, *Sol. Phys.*, **55**, 121

Schwabe, M.: 1844, *Astron. Nachr.*, **21**, 233

Schwenn, R., dal Lago, A., Huttunen, E., Gonzalez, W. D.: 2005, *Ann. Geophys.*, **23**, 1033

Shanmugaraju, A., Moon, Y. J., Dryer, M., Umapathy, S.: 2003, *Sol. Phys.*, **217**, 301

Sheeley, N. R, Jr., Howard, R. A., Michels, D. J., Robinson, R. D., Koomen, M. J., Stewart, R. T.: 1984, *ApJ*, **279**, 839

Sheeley, N. R, Jr., Howard, R. A., Michels, D. J., Koomen, M. J., Schwenn, R., Muehlhaeuser, K. H., Rosenbauer, H.: 1985, *JGR*, **90**, 163

Sheeley, N. R, Jr., Walters, J. H., Wang, Y. M., Howard, R. A.: 1999, *JGR*, **104**, 24739

Shen, C. L., Liao, C. J., Wang, Y. M., Ye, P. Z., Wang, S.: 2013, *Sol. Phys.*, **282**, 543

Smerd, S. F., Sheridan, K. V., Stewart, R. T.: 1974, Coronal Disturbances, IAU Symp, (ed.) G.A. Newkirk, Reidel, Dordrecht, **57**, 389.

Smith, C. W., L'Heureux, J., Ness, N. F. et al.: 1998, *Space Sci. Rev.*, **86**, 613

Srivastava, N., Schwenn, R., Inhester, B., Stenborg, G., Podlipnik, B.: 1999, *Space Sci. Rev.*, **87**, 303

Stewart, R. T.: 1985, Moving type IV bursts, (eds.) D. McLean, N. Labrum, Solar Radiophysics: Studies of Emission from the Sun at Metre Wavelengths, Cambridge University Press, Cambridge, 361

Stone, E. C., Frandser, A. M., Mewaldt, R. A., et al.: 1998, *Space Sci. Rev.*, **86**, 1

Strachan, L., Suleiman, R., Panasyuk, A. V., Biesecker, D. A., Kohl, J. L.: 2002, *ApJ*, **571**, 1008

Sturrock, P. A.: 1966, *Nature.*, **211**, 695

Suzuki, S., Dulk, G. A.: 1985, Solar Radiophysics: Studies of Emission from the Sun at Metre Wavelengths, (eds.) D. J. McLean, N. R. Labrum, (Cambridge, New York: Cambridge Uni. Press), 289-332

Švestka, Z.: 2001, *Space Sci. Rev.*, **95**, 135

Tang, J. F., Wu, D. J., Tan, C. M .: 2013, *ApJ*, **779**, 83

Temmer, M., Veronig, A. M., Vršnak, B., Rybák, J., Gömöry, P., Stoiser, S., Maričić, D., P. A.: 2008, *ApJ*, **673**, L95

Temmer, M., Veronig, A. M., Kontar, E. P., Krucker, S., Vršnak, B.: 2010, *ApJ*, **712**, 1410

Temmer, M., Vršnak, B., Rollett, T., Bein, B., et al.: 2012, *ApJ*, **749**, 57

Torsti, J., Valtonen, E., Lumme, M., et al.: 1995, *Sol. Phys.*, **162**, 505

Torsti, J., Riihonen, E., Kocharov, L.: 2004, *ApJ*, **600**, L83

Tousey, R.: 1973, *Bull. American Astron. Soc.*, **5**, 419

Tsuneta, S., Acton, L., Bruner, M., et al.: 1991, *Sol. Phys.*, **136**, 37

Uchida, Y.: 1960, *Pub. Astron. Soc. Japan.*, **12**, 376

Vainio, R., Agueda, N., Aran, A., Lario, D.: 2007, (ed.) J. Lilensten, Space Weather: Research Towards Applications in Europe, *Astrophys. Space Sci. Library.* **344**, 27

Vourlidas, A., Howard, R. A., Esfandiari, E., et al.: 2010, *ApJ*, **722**, 1522

Vršnak, B., Lulić, S.: 2000, *Sol. Phys.*, **196**, 181

Vršnak, B.: 2001, *JGR*, **106**, 25291

Vršnak, B ,Aurass, H., Magdalenic, J., Gopalswamy, N.: 2001, *A&A*, **377**, 321

Vršnak, B, Maričić, D., Stanger, A. L., Veronig, A.: 2004a, *Sol. Phys.*, **225**, 355

Vršnak, B , Magdalenič, J., Zlobec, P.: 2004b, *A&A*, **413**, 753

Vršnak, B., Warmuth, A., Temmer, M.: 2006, *A&A*, **448**, 739

Vršnak, B.: 2008, *Ann. Geophys.*, **26**, 3089

Vršnak, B., Cliver, E. W.: 2008, *Sol. Phys.*, **253**, 215

Webb, D. F., Hundhausen, A. J.: 1987, *Sol. Phys.*, **108**, 383

Weiss, A. A.: 1963, *Aust. J. Phys.*, **16**, 526

Wild, J. P., McCready, L. L.: 1950, *Aust. J. Sci. Res. A.*, **3**, 387

Wild, J. P., Sheridan, K. V., Neylan, A. A.: 1959, *Austr. J. Phys.*, **12**, 369

Wild, J. P., Smerd, S. F., Weiss, A. A.: 1963, *Annu. Rev. Astron. Astrophys.*, **1**, 29

Winglee, R. M., Dulk, G. A.: 1986, *ApJ*, **307**, 808

Wuelser, J.-P., Lemen, J. R., Tarbell, T. D., et al.: 2004, (eds.) S. Fineschi, M. A. Gummin, Telescopes and Instrumentation for Solar Astrophysics, Proc. SPIE **5171**, 111

Yashiro, S., Gopalswamy, N., Michalek, G., et al.: 2004, *JGR*, **109**, A07105

Yashiro, S., Akiyama, S., Gopalswamy, N., Howard, R.: 2006, *ApJ*, **650**, L143

Zhang, J., Dere, K. P., Howard, R. A., Kundu, M. R., White, S. M.: 2001, *ApJ*, **559**, 452

Zhang, J., Dere, K. P., Howard, R. A., Vourlidas, A.: 2004, *ApJ*, **604**, 420

Zhang, J., Dere, K. P.: 2006, *ApJ*, **649**, 1100

Zimovets, I., Vilmer, N., Chian, A. C. L., Sharykin, I., Struminsky, A.: 2012, *A&A*, **547**, 13

Zucca, P., Pick, M., Demoulin, P., et al.: 2014, *ApJ*, **795**, 15

Annales Universitatis Turkuensis

Turun yliopisto
University of Turku

Painosalama Oy, Turku, Finland 2018

ISBN 978-951-29-7315-6 (PRINT)
ISBN 978-951-29-7316-3 (PDF)
ISSN 0082-7002 (PRINT) | ISSN 2343-3175 (PDF)